Research Square

Preprints are preliminary reports that have not undergone peer review.
They should not be considered conclusive, used to inform clinical practice,
or referenced by the media as validated information.

Molecular and Functional Dysregulations in Novel, Rett Syndrome Patient-Derived Cerebral Organoids

Klaudia M. Braczyk
University of California, Davis
Iliya Y. Voytsyshyn
University of California, Davis
Viktoria Haghani
University of California, Davis
Timothy Fenton
University of California, Davis
Mandeep Singh
University of California, Davis
Camille Loret
University of California, Davis
Peter Beal
University of California, Davis
Roy Ben-Shalom
University of California, Davis
Julian A. N. M. Halmai
University of California, Davis
Kyle D. Fink
kdfink@health.ucdavis.edu

University of California, Davis

Research Article

Keywords:

Posted Date: July 8th, 2026

DOI: https://doi.org/10.21203/rs.3.rs-10208343/v1

License: This work is licensed under a Creative Commons Attribution 4.0 International License.
Read Full License

Additional Declarations: No competing interests reported.

Abstract

Rett syndrome (RTT) is a severe neurodevelopmental disorder (NDD) caused by mutations in *MECP2*. Although existing RTT organoid models recapitulate key disease-associated phenotypes, scalable and patient-relevant platforms for mechanistic and therapeutic studies remain limited. Here, we establish clonal cerebral organoids (COs) derived from patient neural stem cells (NSCs) harboring the R270X mutation to model RTT. Established COs exhibit progressive neuronal maturation, diverse neuronal composition, allele-specific MECP2 expression, and transcriptional dysregulation associated with loss of full-length MECP2 protein. Mutant COs also display reduced organoid size, impaired neurite outgrowth, and altered network activity, consistent with functional neuronal deficits in RTT. In addition, the model supports dose-dependent AAV9 transduction, enabling future evaluation of therapeutic delivery approaches. Together, this work introduces an NSC-derived cerebral organoid platform that captures key molecular and functional features of RTT and provides a scalable, patient-relevant model for mechanistic and therapeutic studies.

Highlights

- Patient NSC-derived cerebral organoids model Rett syndrome across development
- R270X mutation alters full-length MECP2 expression and drives transcriptional dysregulation
- MUT COs show reduced size, impaired neuronal outgrowth and impaired electrophysiological activity consistent with RTT phenotypes
- NSC-derived cerebral organoids can be transduced with AAV9 in dose-dependent manner

Introduction

Rett syndrome (RTT) is a devastating, neurodevelopmental disorder (NDD) predominantly affecting females with prevalence of approximately 1:10,000 female births(1). The majority of the patient population harbor heterozygous mutations in the methyl-CpG-binding protein 2 (*MECP2*) gene located on the X chromosome, encoding the MECP2 protein (2)(3). MECP2 is highly expressed in the central nervous system, including the cerebral cortex, where it has been shown to function as a master epigenetic regulator controlling expression of numerous genes involved in neurodevelopment and neuronal function(4)(5)(6). Individuals with Rett syndrome typically exhibit an initial period of apparently normal development, followed by developmental regression between 12 and 30 months of age(7), characterized by onset of motor and cognitive impairments, repetitive hand movements, seizures and breathing abnormalities(8)(1).

RTT was first reported in 1966 by Dr. Andreas Rett (9), but it wasn't until three decades later that mutations in the *MECP2* gene were identified as the underlying cause of RTT (2). This discovery shifted the field towards further researching the structure and biological role of MECP2 protein, leading to the identification of the most essential MECP2 domains, the Methyl-CpG-binding domain (MBD) and the Transcriptional Repression Domain (TRD), and determination of their roles in methylated DNA binding

and interaction with co-repressor complexes(10)(11). Creation of the first mouse model of RTT (12)(13) allowed for systemic study of the disease and built strong foundations for searching for a cure with an indication that RTT is potentially reversible(14). Since then, RTT has been modeled and studied in various *in vitro* and *in vivo* systems including 2D neurons with CRISPR-engineered, RTT-associated *MECP2* mutations(15)(16), 2D neurons derived from RTT patient's induced pluripotent stem cells (iPSCs)(17)(18)(19), and numerous mouse models(12)(20)(21)(22). Previous studies reported broad transcriptional dysregulation(17)(23), altered neuronal morphology(24)(17)(25), and abnormal electrophysiological activity(16) when mutations in *MECP2* were present. These models have been invaluable for elucidating the bases of RTT physiology, pathology and in pioneering attempts for therapeutic testing.

However, 2D neuronal monocultures often struggle to recapitulate the cellular heterogeneity and microenvironment of brain tissue(26)(27). Further, therapeutic screening in mice is costly, labor-intensive and faces species differences between mouse and human brain anatomy and physiology limiting translatability. Additionally, many novel therapeutic approaches targeting the underlying cause of RTT, like CRISPR-mediated genome editing, epigenetic editing, prime editing platforms, require a human model due to their specificity to the human genome. These obstacles hinder timely delivery of potential therapeutics for complex NDDs, like RTT, to patients, despite the severity of their conditions(28)(29)(30)(31)(32). Limitations of previous experimental systems created the need for more physiologically relevant, patient-specific human brain models. Development of three-dimensional cerebral organoids (COs) has addressed this gap by enabling high-throughput *in vitro* modeling of human brain and brain-like microenvironment(33)(34). COs derived from patient's iPSCs provide an opportunity to recapitulate aspects of early neurodevelopment, can develop diverse neuronal and glia cell populations, and support network-level electrophysiological activity in human brain tissue context, simultaneously enabling application of high-throughput characterization assays and prospect drug screening(35)(36). However, traditional iPSC-derived brain organoids exhibit several limitations, including formation of necrotic cores, inconsistent neuronal firing patterns, and the unintended presence of non-neuronal cell types(37). These challenges created the need for optimized CO systems, such as NSC-derived organoids.

Here we present a RTT patient-derived CO model established using a novel iPSC-to-NSC-to-cerebral organoid protocol. We utilized clonal iPSC lines derived from a RTT patient carrying the heterozygous premature stop codon mutation (c.808C > T; p.R270X) in *MECP2* to differentiate clonal NSC lines, and COs. We evaluated organoid samples at three developmental stages: early development (d18), initial neuronal maturation (d46), and mature neuronal stage (d90 and onwards). We show that our model recapitulates key features of RTT, described in prior models and, with further development, has potential to serve as a system for high-throughput AAV9-based therapeutic screening in the future. In brief, we show increase neuronal maturation and cellular diversity with organoid development, consistent MECP2 allele-specific expression, functionality of full-length MECP2 in the isogenic control, transcriptomic dysregulation, reduced size, impaired neurite outgrowth structure, and dysregulated network activity in mutant organoids, which align with earlier reports in RTT models while also making our platform suitable for scalable, high-throughput therapeutic screening.

Results

NSC-derived COs develop over time with increasing cellular diversity

To validate that our COs accurately model native neurodevelopmental processes, such as neuronal maturation, we isolated RNA from whole organoids at three timepoints (d18, d46 and d90) representing crucial stages of their development in culture (stem cell phase, early neuronal maturation/patterning phase, mature neuronal phase respectively), each supported by respective culture media. We used RT-qPCR to evaluate expression of known neural stem cell, mature neuronal, and glial markers. We observed strong, time-dependent changes in expression levels of these markers, following an expected pattern for neuronal maturation in both isogenic WT and R270X MUT organoids from d18 to d90 in culture. Stem cell marker, *PAX6* (Fig. 1A), showed significant temporal decrease in expression ($p < 0.0001$, $F(2, 29) = 72.55$), consistent with its expected decline as progenitor cells differentiate into mature neuronal cells. In contrast, mature neuronal markers: *MAP2* ($p < 0.0001$, $F(2, 29) = 48.09$(Fig. 1B), *NeuN* ($p < 0.0001$, $F(2, 29) = 108.2$) (Fig. 1C) increased significantly over time in both WT and MUT lines, further supporting consistent organoid neuronal development in culture. Additionally, excitatory neuronal marker *vGLUT2* ($p < 0.0001$, $F(2, 29) = 109.7$) (Fig. 1D), inhibitory neuronal marker *GAD1* ($p < 0.0001$, $F(2, 29) = 127.7$) (Fig. 1E), and glia marker *S100* β ($p < 0.0001$, $F(2, 29) = 127.9$) (Fig. 1F), also showed significant increase in expression with time, supporting desired, increasing cell diversity in developing COs. The genotype effect was limited, yet significantly decreased *PAX6* ($p = 0.0136$) expression was observed in MUT R270X organoids compared to isogenic WT at d46 in culture suggesting a possibility of premature neuronal maturation in the MUT line (Fig. 1A).

NeuN and *S100* β increase in expression with time in culture was further confirmed qualitatively on protein level through immunocytochemistry (ICC) (Fig. 1G). These findings strongly support our maturation protocol, desired progressive neuronal maturation of the CO model, and confirm the presence of multiple neuronal cell types, which opens an avenue for utilizing this model to further study RTT and screen potential therapeutics, not only in one type of neuronal cells, but in diverse neuronal cell populations.

Patient-derived COs show clonal, allele-specific expression of MECP2

Next, we investigated MECP2 expression in the NSC-derived CO lines across multiple stages in development (NSCs before aggregation, and d18, d46, d90 COs). RNA amplicon sequencing across the R270 locus in patient-derived NSCs confirmed allele-specific expression of MECP2 transcripts. WT organoids predominantly expressed the wild-type allele, which accounted for 96.93% of total reads, whereas only 0.33% of reads corresponded to the R270X (c.808C > T) allele. In contrast, MUT organoids predominantly expressed the R270X allele, representing 97.41% of total reads, with no detectable reads

corresponding to the wild-type allele (Fig. 2A). Western blot analysis in COs derived from these clonal NSC lines, revealed presence of full-length MECP2 protein (~ 75 kDa) only in WT organoids and absence of full-length MECP2 in MUT organoids at d18, d46 and d90 in culture (Fig. 2B). Consistently, ICC showed full-length MECP2 protein expression in WT COs with no detectable signal in MUT organoids at the same times in development. Interestingly, we observed changes in localization of the MECP2 signal within the WT organoid structures with time in culture. At early development (d18), MECP2 expression appears more evenly dispersed across the organoid structure, with gradually increasing, to strong nuclear co-localization within mature neurons (NeuN-positive cells) at d90 in development (Fig. 2C). Together, this data confirms clonal, continuous, allele-specific MECP2 expression consistent with the clonal design of this patient-derived CO model for RTT phenotype characterization and future functional protein rescue studies.

Full-length MECP2 in isogenic WT COs binds previously reported gene targets

To assess physiological functionality of MECP2 in our model, we performed ChIP-qPCR using WT isogenic and MUT R270X COs. We demonstrated MECP2 occupancy at previously reported(38) MECP2-occupied *loci* in WT organoids compared with IgG control at *BDNF* ($p = 0.0188$, $F(3, 8) = 6.04$), *CRMP1* ($p < 0.0001$, $F(3, 7) = 271.3$), *GNB1* ($p < 0.0001$, $F(3, 8) = 57.92$), and *DYNAMIN* ($p = 0.0124$, $F(3, 8) = 7.04$) (Fig. 3). These findings support the functionality of full-length MECP2 in WT organoids. Additionally, consistently with the absence of full-length MECP2 protein previously demonstrated in the R270X MUT CO line, no MECP2 binding was detected in MUT COs using a C-terminus-binding ChIP antibody.

MECP2 deficiency is associated with widespread transcriptomic dysregulation and an altered neurodevelopmental trajectory

To further understand complex transcriptomic changes associated with lack of full-length MECP2 and investigate potential RTT-associated pathway dysregulations in our model we utilized bulk RNA sequencing (RNAseq) and focused our analysis on neurodevelopmental trajectories and temporal gene expression changes between genotypes. We sequenced and analyzed data from CO samples at three developmental stages: early development (d18), initial neuronal maturation (d46), and mature neuronal stage (d90). First, we observed visible and consistent clustering of the biological replicate samples from independent organoid aggregations at each time point in development from separate organoid aggregations in heatmaps, suggesting batch-to-batch consistency and reproducibility. We also observed strong developmental stage-driven clustering, suggesting distinct gene expression signatures between three developmental timepoints with strongest diversification between d18 and d90 samples, and transitional signatures for d46 organoids in both WT and MUT COs, which support general developmental changes in COs with time in culture (Fig. 4A). Distinct transcriptomic signatures were further confirmed with PCA analysis, where clustering by developmental stage was observed (Fig. 4B).

To further explore the allele-driven gene signature changes in our model, we carried out a differentially expressed gene (DEG) analysis on MUT vs. WT organoid samples, which identified total of 120, 91, and 66 significant DEGs (Adjusted p value $\leq$ 0.05) on d18, d46 and d90 respectively. Gene ontology analysis (GO) for the significant DEGs at each developmental stages revealed progressive, allele-driven dysregulation. At d18, we observed general gene expression impairments reflected in enriched terms for developmental and cellular organization pathways including cilium assembly, microtubule anchoring, small-molecule metabolism, nucleotide metabolism, mitochondrial enzymes activity, nucleic acid binding, but also initial neurodevelopment impairment with GO terms enriched in negative regulation of nervous system development, and cell proliferation in forebrain **(**Fig. 4C**)**. In the initial neuronal differentiation stage at d46, the transcriptional profile showed further enrichment in mitochondrial metabolism and nucleic acid processing pathways, including sequence-specific DNA and mRNA binding. In parallel we observed enrichment in pathways related to synapse structure, ion transport (with the emphasis on potassium channel physiology), cell junction organization, as well as neurite and axonal projection. Together these changes highlight the trajectory of mutation-driven transcriptional changes transitioning from general cellular processes, progressing towards impaired neuronal maturation, morphology and function **(**Fig. 4D**)**. On d90, we continued to observe strong enrichment in terms associated with potassium channels and potassium ion transport, which might suggest progressive dysregulation in neuronal cell electrophysiology. This is consistent with previously reported impaired potassium channel activity in astrocytes of RTT mouse model that has been connected to affected neuronal activity in MECP2-deficient mice(39). We also observed enrichment in fatty-acid and lipid metabolism, as well as oxidoreductase pathways **(**Fig. 4E**)**. This suggest that later-stage mutant organoids capture not only neuronal abnormalities, but also metabolic and redox dysregulation recognized as part of the known RTT pathophysiology(40)(41). Taken together, the MUT organoids display progressive, mutation-driven, temporal transcriptomic changes starting as general cellular function dysregulations and initial neurodevelopmental impairments at early stage in CO development, followed by initial abnormalities in mitochondrial metabolism, neuronal physiology and synaptic functions in middle-stage organoids, progressing into complex metabolic and redox impairments in mature organoids. This trajectory is consistent with disease progression in early stages of RTT, and further support our model's ability to recapitulate key molecular aspects of the progressive neurodevelopmental dysregulations in RTT.

Mature MUT R270X organoids exhibit reduced size and disrupted neurite outgrowth

To further investigate structural differences between WT and MUT COs, we measured organoid area at day 129, a stage at which organoid growth had largely stabilized. We observed significant differences in size between the WT and MUT COs (Fig. 5A). Brightfield area quantification revealed significantly decreased organoid size in MUT COs relative to the isogenic WT line at d129 in culture (WT: 1,031,944 μm², n = 121; MUT: 881,522 μm², n = 120; Welch's two-tailed t-test: $t(213.8) = 4.28$, $p < 0.0001$; mean difference [WT-MUT] = 150,423 μm²) (Fig. 5B).

Next, we performed the neurite outgrowth assay to investigate potential mutation-driven morphological changes in neurons building the COs. Neurites in the MUT CO outgrowth showed visibly overlapping projections and reduced orderly extensions (Fig. 5C) with decreased number of intersections per µm of radius compared with isogenic WT, data presented as mean ± standard error of the mean (SEM) (Fig. 5D). Data was analyzed using a newly developed Sholl analysis tool: Data Engine of Rapid Urban Neural Yields tool (DERUNY). Neurite branching differences were assessed with the Mann–Whitney U test (Fig. 5E). A total of 66 fluorescence images were analyzed (n = 33 per group, WT and MUT), with three images acquired per organoid from 11 COs in each group.

Mutant organoids show altered burst organization and reduced outside-burst inter-spike interval

To assess the electrophysiological phenotype in our RTT CO model, we performed High-Density Microelectrode Array (HD-MEA) recordings on mature WT (n = 11) and MUT R270X (n = 12) COs at d110 in culture, after neuronal maturation had been confirmed by robust expression of mature neuronal markers at day 90. We recorded and analyzed activity at day *in vitro* 7, 14, and 21 after plating on the MEA chip (DIV7, DIV14, DIV21). Representative active area plots confirmed proper attachment and neurite outgrowth in both WT and MUT R270X organoids (Fig. 6A). Raster plots and network activity traces demonstrated robust network activity in both organoid lines (Fig. 6B, 6C**)**. WT organoids displayed regular discrete bursting events whereas MUT organoids exhibited broader and less consistent burst structure with more dispersed activity between bursts which showed a resemblance to reverberating super-burst (RSB) patterns previously reported in RTT neurons(16) (Fig. 6B, 6C, 6D). For d7 only, recordings with active area below 1% were excluded from subsequent quantification because activity was too sparse for reliable network-level measurements resulting in decreased replicates (WT n = 6, MUT n = 3). We then quantified activity metrics and discovered no significant genotype differences between WT and MUT R270X in active area (d7 p = 0.693; d14 p = 0.709; d21 p = 0.863), mean firing rate (d7 p = 0.263; d14 p = 0.401; d21 p = 0.662), or mean spike amplitude (d7 p = 0.886; d14 p = 0.616; d21 p = 0.580) (Fig. 6E.**i-iii**). When analyzing network bursting behavior, we observed significantly decreased Mean Outside Burst Inter-Spike-Interval in MUT COs at d14 (p = 0.043) and p21 (p = 0.002), but not at d7 (p = 0.933), consistent with increased spiking outside of burst events as networks matured (Fig. 6E.**iv**). This pattern is similar to observations of the RSB pattern in previously reported RTT neuron studies(16). Statistical significance between wild-type (WT) and mutant (MUT) groups at each time point (DIV 7, 14, and 21) was determined using a one-way ANOVA. All results are presented as mean ± SEM, with significance defined as $p < 0.05$.

Patient-derived organoids are transduced in dose-dependent manner with AAV9

Currently studied therapeutics targeting the underlying cause of RTT are strongly focusing on utilizing adeno-associated virus (AAV) as a delivery vehicle(42)(43). Therefore, to evaluate our model's

applicability in dose-dependent screening of prospective therapeutics using AAV delivery systems, we transduced the MUT COs and the isogenic WT COs with three doses (viral genomes, vg) of the in-house-made AVV9 carrying GFP (AAV9-GFP) reporter at low (1 x 10^{11} vg), mid (1 x 10^{12} vg) and high (1 x 10^{13} vg) dose per group. After 24 days post-transduction, genomic DNA (gDNA) was isolated from single organoids (n = 3 COs per group) and used to perform qPCR with primers specific to the GFP transgene to determine transduction efficiency. Relative GFP signal was normalized to GAPDH (relative vg) and showed increase in a dose-dependent manner, with high-dose treatment resulting in a significant increase compared to untreated, low, and mid-dose conditions (two-way ANOVA with Šídák's multiple comparisons test, $p < 0.0001$), while no significant differences were observed between untreated, low, and mid doses. Additionally, no significant differences in relative viral genomes were observed between WT and MUT COs groups at any treatment dose (two-way ANOVA with Šídák's multiple comparisons test; untreated $p > 0.9999$, low $p > 0.9999$, mid $p = 0.9924$, high $p = 0.4132$) (Fig. 7A).

To evaluate distribution of the virus within the organoid structure, we performed whole-organoid immunocytochemistry with Z-stack projection. Consistent with GFP transgene levels quantified by qPCR, WT COs treated with the high AAV dose exhibited abundant GFP-positive cells throughout the imaged three-dimensional organoid structure. GFP signal colocalized with MAP2-positive mature neurons, supporting efficient transduction of mature neuronal populations within the model. (Fig. 7B).

Discussion

Neurodevelopmental disorders, including RTT, are highly complex and remain challenging to study using traditional *in vitro* experimental models. Consequently, there is a growing need for optimized, patient-relevant platforms that faithfully recapitulate key aspects of the human brain microenvironment while supporting efficient and translational evaluation of therapeutic candidates. To address this need, we utilized clonal patient iPSC-derived NSCs harboring a R270X premature stop codon mutation, representative of one of the most prevalent mutation types in the RTT patient population, together with a newly optimized neuronal maturation protocol to establish RTT-like cerebral organoids. We comprehensively characterized the model across multiple molecular and functional features, including neurodevelopmental progression, cellular composition, clonal MECP2 expression patterns in MUT and isogenic WT control organoids, MECP2 target engagement in isogenic COs, pathway-level transcriptional dysregulation, altered organoid growth and neurite organization, and disrupted neuronal network activity. Furthermore, we demonstrated compatibility of the model with AAV9-mediated transduction, supporting its future application in the evaluation of genetic cargo delivery and other therapeutic strategies.

Evaluation of neuronal maturation and cellular composition in our CO model revealed a progressive decrease in the neural progenitor marker *PAX6* and increase in expression of mature neuronal and glial markers (*MAP2, NeuN, vGLUT2, GAD1*, and *S100β*). These findings indicate that our COs follow expected neurodevelopmental trajectories, consistent with previous brain organoid studies(44)(45)(46), while generating a heterogeneous neuronal and glial cell population. Interestingly, we observed significantly lower PAX6 levels in MUT organoids at d46 compared with WT controls, suggesting a potential

impairment in neural progenitor populations during early organoid development, a phenotype previously reported in RTT organoid models(47). Progressive neuronal maturation and cellular diversity were further confirmed by qualitative immunocytochemical analyses. Collectively, data from multiple complementary assays support the progressive maturation of our RTT CO model over time in culture and demonstrate the establishment of a diverse cellular composition that, to a degree, resembles the complexity of the human brain microenvironment.

Next, we investigated allele-specific MECP2 expression in R270X MUT and isogenic WT CO lines to confirm the durability of clonal MECP2 expression throughout organoid development. Using RNA amplicon sequencing, western blotting, and immunocytochemistry, we consistently detected full-length MECP2 expression in WT organoids, whereas full-length MECP2 was absent in the MUT line. These findings are consistent with previous studies demonstrating reduced stability and loss of full-length MECP2 protein resulting from nonsense mutations(48)(49)(50). Confirmation of stable, clonal MECP2 expression was critical, as many RTT-associated phenotypes depend on the presence and functionality of full-length MECP2. Moreover, the absence of detectable full-length MECP2 in the MUT line establishes a well-defined platform for MECP2 reactivation studies, enabling precise assessment of full-length MECP2 restoration and following downstream phenotypic rescue.

To evaluate the physiological functionality of MECP2 in our organoid model, we performed a target engagement study using ChIP-qPCR. We detected MECP2 occupancy at the *BDNF*, *GNB1*, *DNM1*, and *CRMP1* loci in isogenic WT organoids, whereas occupancy was reduced to background levels in MUT COs. These findings are consistent with previous ChIP studies using post-mortem RTT patient and healthy control brain tissue, which reported similar patterns of MECP2 binding at these loci(51), and provide functional evidence of MECP2 activity in our isogenic WT line. Importantly, the absence of detectable binding in MUT COs most likely reflects the loss of full-length MECP2, as target engagement was assessed using a C-terminus-binding antibody.

To gain insight into transcriptome-wide dysregulation associated with the R270X mutation, we performed RNA sequencing across multiple stages of CO development. Broad differential gene expression was observed between isogenic WT and MUT COs throughout maturation, affecting numerous pathways previously implicated in RTT. Samples clustered according to developmental stage, demonstrating reproducible organoid maturation across independent aggregations. Importantly, RTT-associated transcriptional abnormalities evolved throughout CO development. Early-stage organoids (d18) exhibited dysregulation of general cellular and gene regulatory processes, whereas early maturating organoids (d46) showed more pronounced neuronal and synaptic alterations. In mature COs (d90), transcriptional changes were enriched for pathways related to electrophysiological function, particularly ion channel activity, alongside disruptions in redox and lipid metabolism. Together, these findings suggest that our model recapitulates the progressive molecular alterations associated with RTT and provides a platform for future mechanistic and therapeutic studies.

Interestingly, we observed reduced organoid size in the R270X MUT line relative to isogenic WT controls. Although the mechanisms underlying this phenotype remain unclear, several possibilities may contribute, including impaired cell survival, reduced neuronal soma size, or impaired neural progenitor populations. The latter may be linked to the significantly reduced expression of the neural progenitor marker PAX6 observed at day 46 in R270X MUT organoids and abnormalities in neural progenitor populations have also been reported in other RTT organoid models(47), further supporting this potential mechanism. However, additional studies will be required to determine whether impaired neural progenitor populations directly contribute to the reduced organoid size observed in our model.

In connection to the RNAseq findings on neuronal impairments in MUT organoids, we investigated structural changes in neurons within the organoids by comparing neuronal outgrowths between MUT and WT COs. The assay revealed more overlapping neurites with lower number of intersections per µm in the MUT COs. This reflectes significantly disrupted radial organization of the neurite outgrowth, whereas neurite outgrowth of isogenic WT organoids extended more uniformly from the organoid body with minimal overlapping. This finding is consistent with previously reported abnormal neuronal structures in RTT organoids (47) and supports our organoid model's potential to recapitulate structural neuronal impairments associated with RTT. Driven by the lack of availability of appropriate tools to faithfully quantify high-density neurite outgrowths, we developed a novel Sholl analysis-based tool, DERUNY, that allows for rapid quantification of high-density neurite outgrowths and statistical comparison between groups. This tool will be offered as an open access, online tool to support future studies on high-density neurite outgrowth quantification in the field.

Observed electrophysiological changes on the neuronal network level in HD-MEA, where R270X MUT organoids showed decreased mean outside-burst ISI compared to isogenic WT at DIV14 and DIV21, suggest shorter quiescent periods between bursts and increased background spiking activity consistent with altered network organization. Representative MUT recordings also displayed broader and less synchronized burst events with more reverberant activity between bursts than WT recordings. However, because active area, mean firing rate, and spike amplitude did not differ significantly between genotypes across time points, these findings are interpreted as altered burst organization and increased inter-burst spiking rather than a generalized hyperexcitability. Accordingly, the observed reverberant events are best described as RSB-like, or as resembling previously reported RTT network phenotypes, rather than as definitive reverberating super-bursts. This network behavior might be connected to the downstream changes of loss-of-function mutations in *MECP2*. Taken together, these results suggest that our organoid model may be capable of recapitulating differences in network behavior resulting from R270X mutation in MUT COs. Future studies on this model should include testing for potential phenotype rescue.

Finally, we show dose-dependent transduction of RTT-patient-derived COs with AAV9 carrying reporter cargo. We observed dose-dependent transgene delivery, with no significant differences in delivery between MUT vs WT organoids. This observation, serves as an important connection between disease modeling and applicability in potential therapeutic screening, positioning our model as a scalable, high-

throughput, human patient, and brain tissue-relevant platform for screening therapeutics delivered through AAVs.

In conclusion, we show that RTT-patient derived COs established using our new NSC-based protocol follow expected neurodevelopmental trajectory and exhibit diverse neuronal cell population needed for recapitulation of patient's brain environment. We showed progressive, disease-relevant transcriptomic dysregulation following developmental trajectory of Rett syndrome. Further, we demonstrated across multiple independent assays that loss of full-length MECP2 in our model associate with reduced organoid size, impaired neurite outgrowth, and dysregulated network activity. These results are in accordance with multiple previously reported neuronal impairments in mouse and human RTT models(25)(16)(52). Lastly, we show potential of this model in AAV9-based therapeutic screening through successful, dose-dependent transduction.

Although COs are a promising platform to study complex NDDs, like RTT, and great progress has been made in optimizing them to study NDDs, as exemplified by our findings, the field still faces some challenges, and it is important to acknowledge that no model is perfect. In our case, we wanted to highlight the future need for more in-depth characterization and mechanistic studies, as well as inclusion of additional RTT patient iPSC lines harboring various types of mutations (e.g. microdeletions, substitutions), and investigating their influence on the phenotype in this model. Additionally, following up on the RNAseq data with the single-cell RNAseq analysis from our COs in the future, would provide higher-resolution data and highlight cell-type-specific dysregulation mechanisms that might be less refined in bulk RNAseq data. Finally, screening of various types of current drug candidates for RTT (e.g. small molecule drugs, oligonucleotide drugs, epigenetic-based therapy, gene therapy) in our model will be highly beneficial to confirm model's versatility across multiple therapeutic approaches. Our current application of this model is to test potential therapeutics, and for this, we highly value the clonal aspect of this model. We also consider deriving mosaic organoid lines and assembloids in the future, utilizing both isogenic WT and MUT expressing lines to specifically study cell-non-autonomous mechanisms previously reported to play role in RTT(53).

Materials and Methods

Overview

We compared isogenic (WT) and R270X (MUT) CO lines across molecular, structural, and functional readouts at day 18 (d18), 46 (d46) and 90 (d90) post-aggregation in culture. Separate batches correspond to individual aggregations of organoids from NSCs. Biological replicates were independent wells of organoids from one aggregation (batch) unless stated otherwise. Technical replicates come from the same sample originating from the same well from the same batch. Sample sizes were chosen based on prior experience, variance estimates, and feasibility.

iPSC-Derived Neural Stem Cells

RTT iPSCs (2043iPS-D-WT*0 and 2043iPS-A-MUT*0: c.C808T; R270X) were obtained from the Rett Syndrome Research Trust (RSTR) iPSC collection at the Coriell Institute. The iPSC lines were cultured in StemFlex (Gibco) medium on Matrigel (Corning) coated 6-well culture plates, with media changed every 48h. NSCs were generated through EBs formation on Aggrewell 800 (StemCell Technologies) for 24 hours before plating onto Ultra-Low Attachment dishes (Corning) in EB medium (Knockout DMEM/F12 (Gibco) and 15% KSR (Gibco) plus 100x NEAA, 100x Glutamax & 0.55mM 2-Mercaptoethanol) for 3 days; media was changed at 48h. On days 2, 4 and 5 of starting differentiation, EB media was supplemented with 500ng/mL Noggin (R&D Systems) and 10uM SB431542 (Tocris). EBs were plated onto GFR Matrigel (Corning) in EB media to promote rosette formation. At 24h, media was changed to NPC Medium (Neurobasal Medium (Gibco) supplemented with Glutamax, NEAA, 1% Pen/Strep, 1% N2 & 20ng/mL bFGF) for 5–6 days and media was changed every 48h. To obtain NSCs, on day 11–12, rosettes were passaged as single cells using Accutase (Sigma) and plated on Poly-L-Ornithine/Laminin (Sigma) coated culture plates in NSC media (NPC media plus 0.1% B27, 20ng/mL EGF, 10mg/mL Insulin & 1.6% D-Glucose). NSCs were then frozen down for later use in NSC freezing medium (NSC medium + 10% DMSO) or cultured further in NSC media. NSC at passages between 6 through 9 were used to establish each batch of the COs.

Cerebral Organoids

On Day 0, NSCs were resuspended in Embryoid Formation Medium (STEMCELL Technologies #5893) at three million cells per aggregation well and aggregated into embryoid bodies using AggreWell 800 (STEMCELL Technologies #34815). After 24h (on Day 1), the embryoid bodies were carefully dislodged from the AggreWell and transferred into 6-well ultra-low attachment plates (Corning #07-200-601) in NSC medium. Partial changes were performed daily until Day 6 (2/3 medium change). From Day 7 to Day 17, NSC medium was changed every other day. On Day 18, all medium was changed to the patterning (LcAMP) medium (Neurobasal Medium (Gibco #21103049) supplemented with 20 µM cAMP (Sigma-Aldrich #D0627-1G), 142 µM ascorbic acid (Bio-Techne #4055/50), 10 ng/µL BDNF (Gibco #45010100UG), 10 ng/µL GDNF (Gibco #45002100UG), 10 ng/µL NT-3 (Gibco #450-03-10UG), 1% GlutaMAX (Gibco #35050061), 1% MEM non-essential amino acids (Gibco #11140050), 1% Penicillin/Streptomycin (Corning #30-002-Cl), N-2 supplement (Gibco #17-502-001), and 2% B-27 supplement (Gibco #17504001). LcAMP media changes were continued every other day until Day 46. On Day 46, the medium was changed completely to the BrainPhys Complete medium (Maturation Media) (BrainPhys Neuronal Medium (STEMCELL Technologies #05790) supplemented with 1 mM cAMP, 2 mM ascorbic acid, 20 ng/mL BDNF, 20 ng/mL GDNF, 1% GlutaMAX, 1% MEM non-essential amino acids, 1% Penicillin/Streptomycin, 2% N21-MAX (Bio-Techne #AR008), 1% Chemically Defined Lipid Concentrate (Gibco #11905031), 0.001 mg/mL mouse laminin (Gibco #23017015), and 1% N2-Plus (Bio-Techne #AR003)), and media changes were performed three times per week until Day 90 and onwards.

Reverse Transcription Quantitative polymerase chain reaction (RT-qPCR)

Multiple organoids were collected at d18, d46 and d90 (in biological triplicate per line, across two batches), washed with 1x phosphate-buffered saline (PBS) and lysed using TriZol Reagent (Invitrogen) with homogenization. RNA was extracted with the Direct-zol RNA Miniprep kit (Zymo Research, #R2052) and analyzed using spectrophotometer for concentration and purity. The RNA was used for reverse transcription reaction with iScript cDNA Synthesis kit (BioRad, #1708890) following the manufacturer's guidelines. Quantitative PCR (qPCR) was performed using: 20ng of cDNA per reaction, 5 µM of primers (**Supplementary Table S1**), and SYBR Green Master Mix (Thermo Fisher Scientific, # A46109) were used for quantitative PCR with the StepOne Plus Real-Time PCR system (Thermo Fisher Scientific). RT-qPCR was performed on biological and technical triplicates. Relative expression analysis was calculated as the delta CT between housekeeping (human β-Actin) and the target gene transcript levels. All data are presented as mean $\pm$ SEM.

Immunocytochemistry

Multiple organoids were collected at d18, d46 and d90 (in biological triplicate per line), washed with 1x PBS and fixed in 4% paraformaldehyde (Bioworld, #30450002) for 22min, at room temperature, shaking. The fixative was removed, and organoids were washed three times with 1x PBS and moved into sucrose solution (30% sucrose in 1x PBS) for 48h, at 4°C, shaking. After 48h, organoids were embedded in OCT-sucrose (22.5ml 100% OCT + 17.5ml 30% sucrose solution; Tissue-Tek® O.C.T. Compound, Sakura, #4583), frozen at -80°C. Organoids were serially cryosectioned at 20 μm thickness per section and mounted onto microscopy glass slides (FisherBrand; #22-037-246). Each microscopy slide with organoid sections was washed three times for 5 minutes with 1x PBS to remove the remaining sucrose-OCT. Each organoid section set was then circled with the ImmEdge Hydrophobic barrier PAP pen (Vector Laboratories, #VEC-H-4000) and air-dried. Blocking and permeabilization was done simultaneously using 50ul of Blocking Solution (10% Normal Goat Serum (Abcam, #ab7481) in 0.1% Triton-X-100 (Sigma-Aldrich, #T8787) in 1x PBS) per section group for 1h at room temperature. Primary antibody incubation was done via antibody multiplexing at optimized dilutions (**Supplementary Table S2**) in Blocking Buffer overnight, at 4°C in humidity chambers. The next day, primary antibodies were removed, and organoid sections were washed three times with 1x PBS. Secondary antibody incubation was also performed via antibody multiplexing at optimized dilutions (**Supplementary Table S3**) for 1h at room temperature in dark, followed by three washes with 1x PBS. Hoechst staining (1:2,000 in 1x PBS) was performed for 10min at room temperature in the dark, followed by three washes with 1x PBS. Sectioned were then air-dried completely and slides were mounted using Fluoromount Aqueous Mounting Medium (Sigma-Aldrich, # F4680), covered with a cover slip and sealed.

Images were acquired across multiple fields within each sample with inverted microscope (Axio Observer 7, Carl Zeiss Microscopy GmbH) at 10x magnification, using 350nm, 488nm, 594nm and 647nm channels, with matched settings across WT and MUT at all timepoints.

Amplicon sequencing

Total RNA was isolated from WT and MUT R270X NSCs with Direct-zol RNA Miniprep kit (Zymo Research, #R2052) following manufacturer's instructions. cDNA was synthetized using RevertAid First Strand cDNA Synthesis Kit (Thermofisher, #K1621) with random hexamer primers according to the manufacturer's guidelines. Nested PCR was performed on the cDNA template first obtaining 1kbp amplicon, then using this amplicon as a template for the second PCR reaction obtaining 207bp amplicon. DNA product was purified post-synthesis with QIAquick PCR Purification Kit (Qiagen, #28104) and sent out for Next-Generation Sequencing to Massachusetts General Hospital DNA Core. Alignment and analysis were performed and visualized using CRISPResso2 tool. Allele fractions (WT vs MUT c.C808T) were computed per sample and reported as percentage of total reads and number of reads.

Western Blot

Multiple organoids were collected per sample at d18, d46 and d90 (in biological triplicate per line) and washed with 1x PBS then lysed in protein lysis buffer (RIPA Lysis and Extraction Buffer (Thermo Scientific, #89901), 1% 2-mercaptoethanol, 1% Halt Protease and Phosphatase Inhibitor Cocktail (Thermo Scientific, #78442). Protein lysates were quantified with Pierce BCA Protein Assay Kit (Thermo Scientific, #10678484) and 20µg of protein lysate was loaded per line of each 4%-20% Stacking TGX Gel (BioRad, Hercules, #4561096EDU), then electrophoresed for 3 hours at 90V and transferred onto methanol-activated Invitrolon PVDF membrane (Thermo Fisher Scientific, #LC2005) overnight at 30V on ice. The next day, membranes were blocked for 1 h at room temperature with 10% SEABLOCK (Thermo Fisher Scientific, #37527) in 0.1% TBST, then incubated overnight with primary antibodies (**Supplementary Table S4**) in 5% SEA BLOCK in 0.1% TBST. The next day, membranes were washed 3 times with TBST, and subsequently incubated with secondary antibodies (**Supplementary Table S4**) in 5% SEABLOCK in 0.1% TBST for 1 hour. Membranes were washed three times with 0.1% TBST and imaged using Odyssey CLx (LI-COR, Lincoln, NE, United States) at 700nm and 600nm channels.

Chromatin Immunoprecipitation- quantitative polymerase chain reaction (CHIP-qPCR)

Organoids were collected at d60 in culture (> 20 organoids per sample, in biological triplicate per line), washed one time with 1xPBS and crosslinking of chromatin was performed for 10min, at room temperature, shaking with crosslinking solution (54ul of 37% Formaldehyde (Sigma-Aldrich, #252549) + 2ml Opti-MEM media (Gibco, #15392402) per 40 organoids) in a well of a 6-well Ultra-Low Attachment plate (Corning). Crosslinking solution was removed and one wash with ice cold 1xPBS was performed. Then 2ml of ice-cold glycine buffer (1ml 500mM Glycine in 1x PBS; Sigma-Aldrich, #W328707) was added to the well with organoids and incubated on a shaker for 5min at room temperature. Glycine buffer was removed, organoids were washed one time with ice-cold 1xPBS and transferred in PBS to 1.5ml Eppendorf tube. Sample were then processed with ChIP-IT Express Chromatin Immunoprecipitation Kit (Active Motif, #53009) according to the manufacturer's instructions. Briefly, ice-cold Complete Lysis Buffer (Lysis Buffer supplemented with PMSF and PIC) was added to crosslinked organoids and incubated for 30min on ice. Next, organoids were homogenized and sonicated on ice: 2 cycles of 5 seconds on, 5 seconds off at 20kHz (FisherScientific, Sonic Dismembrator, Model100).

Presence of released nuclei was confirmed using bright-field microscopy. Samples were span down at 4°C, 5,000 rpm for 10 minutes. Supernatant was discarded and the pellet was used for further CHIP steps. Complete Digestion Buffer (Digestion Buffer with PIC and PMSF) was added to each sample and chromatin shearing was performed for 12 minutes at 37°C with vortexing every 2 minutes. Reaction was stopped by adding ice-cold EDTA and chilled for 10 minutes on ice. Chromatin shearing quality control was performed by adding provided RNAze, and purifying DNA (QIAquick PCR Purification Kit (Qiagen, #28104) to run agarose gel electrophoresis (1% agarose gel, run for 45 min at 120V, BioRad) and visible bands around 100bp were observed for all sheared chromatin samples. Next, sheared chromatin was incubated with mixture of magnetic beads, PIC and CHIP Buffer I with either anti-MECP2 (Diagenode, #C15410052 at 1.5µg per 230µl chromatin sample) or anti-IgG control (Abcam, #Ab46540 at 1.5µg per 50µl chromatin sample), overnight at 4°C, rotating. The next day, the beads were washed according to the manufacturer's instructions, and chromatin was eluted. Reverse crosslinking was performed on the samples and input control was treated according to the manufacturer's instructions. All samples were incubated at 65°C overnight. Next all samples were treated with Proteinase K (provided in the kit) for 1h at 37°C, then reaction was stopped with Proteinase K Stop solution (provided in the kit). All samples were column-purified QIAquick PCR Purification Kit (Qiagen, #28104), concentration of DNA was determined by spectrophotometry. Quantitative polymerase chain reaction (qPCR) was performed using 1µl of purified DNA per reaction, 5µM of primers (**Supplementary Table S5**), and SYBR Green Master Mix (Thermo Fisher Scientific, # A46109) with the StepOne Plus Real-Time PCR system (Thermo Fisher Scientific). Relative expression analysis was calculated as the delta CT between input control and the target genes transcript levels, normalized to the chromatin amounts used for antibody incubation, and further to purified DNA concentrations used for qPCR.

Each locus (*BDNF, GNB1, DNM1, CRMP1*) was analyzed for four groups: MECP2 WT, MECP2 MUT, IgG WT, IgG MUT (in 3 biological replicates, each across multiple organoids per sample). Briefly, Ct values were first converted to % input (used formula: $100 \times 2^{(\mathrm{Ctinput} - \mathrm{CtImmunoPrecipitation})}$), results reported as $\pm$ SEM. GraphPad Prism was used for data plotting and statistics. One-way ANOVA was used for each locus individually across the four groups. Tukey's multiple-comparison tests were performed, with adjusted P values, for the following pairwise comparisons: MECP2 WT vs IgG WT; MECP2 WT vs MECP2 MUT; MECP2 MUT vs IgG MUT. For CRMP1, one outlier datapoint (for MECP2 WT dataset) was excluded prior to data plotting and ANOVA analysis due to technical and QC failure.

RNA Sequencing and Analysis

RNA-seq analysis was conducted using established protocols(54). Briefly, raw reads were trimmed using Trim Galore(55) (v0.6.10), aligned to hg38 using STAR(56) (v2.7.11a), indexed using Samtools(57) (v1.21), and subject to quality control using MultiQC(58) (v1.29). After mapping gene names to HUGO nomenclature and normalizing counts per Chen et al. 2016(59), differential expression between genotype and time point conditions was assessed using limma(60) (3.62.2) and edgeR(61) (v4.4.2). The analyzed groups included: MUT d18 (n = 6), MUT d46 (n = 4), MUT d90 (n = 6), WT d18 (n = 6), WT d46 (n = 5), and WT d90 (n = 5). Gene ontology (GO) was conducted for the significantly differentially expressed

genes per comparison using the GO Biological Process 2025, GO Cellular Component 2025, GO Molecular Function 2025 Enrichr(62) (v3.4) databases.

Heatmaps were generated from z-score normalized read counts to visualize relative gene expression patterns across all samples, with Euclidean distance used for hierarchical clustering of both genes and samples. PCA was performed on normalized gene counts to assess global expression variation, with samples clustered by genotype and time point.

The following additional packages were used to conduct the DEG analysis and visualize results: Jupyter Notebook(63) (v7.4.0), R(64) (v4.4.2), IRkernel(65) (v1.3.2), ggplot2(66) (v3.5.2), tidyr(67) (v1.3.1), dplyr(68) (v1.1.4), polars(69) (v1.30.0), pandas(70) (v2.2.3), seaborn(71) (v0.13.2), matplotlib(72) (v3.10.6), numpy(73) (v1.26.4), rtracklayer(74) (v1.66.0), gplots(75) (v3.3.0), RColorBrewer(76) (v1.1.3), openxlsx(77) (v4.2.8), readxl(78) (v1.4.5), glue(79) (v1.8.0), and ggrepel(80) (v0.9.6).

Area Quantification

Brightfield images of COs were acquired at d129 in culture using EVOS FL Digital Inverted Fluorescence Microscope (Invitrogen) at 4x magnification and identical exposure across all samples (N_{WT}=120 (WT) and N_{MUT}=121; where N is a technical replicate from the same aggregation batch). ImageJ/Fiji (NIH, Bethesda, MD, United States) was used to quantify the areas of the organoids. First, organoid images were converted to 8-bit and a uniform intensity-based threshold was applied to isolate the dark organoid region from the lighter background. Each organoid area (μm²) was quantified through circulating single organoid and using the “Analyze” function. Pixel-to-distance calibration was done based on the microscope photo scalebar. Thresholding parameters were kept constant across samples. Statistical significance was assessed using an unpaired t-test, and data is presented as mean with min-max error bars.

Neurite outgrowth assay

COs at d120 in culture were plated on Poly-L-Ornithine/Laminin (Sigma) coated 24-well culture plates (Corning, # CLS3526) (N_{WT}=11 (WT) and N_{MUT}=11, where N is a technical replicate from the same aggregation batch). Laminin was removed from the wells and organoids were placed on the well’s surface with a P1000 pipette (with previously cut tip) and SUGI absorption spears (AgnThos #18105-01) were used to fully absorb surrounding media. Each organoid was left for three minutes on the well’s surface before adding 50μl Maturation Media to each well with the organoid. Next, the plate was incubated at 37°C and 5% CO2 in the cell culture incubator for 30min before slowly and steady adding an additional 500μl of Maturation Media to each well. Organoids were incubated at 37°C and 5% CO2 in the cell culture incubator for 72h without media change. Next, all media was removed from the wells, one 1xPBS wash was performed, and organoid were fixed with 4% paraformaldehyde for 20min at room temperature. One wash with IHC Wash Buffer (Invitrogen, #00-4954-56) was performed. Next, organoids were treated with permeabilization solution (0.1% Triton-X-100 (Sigma-Aldrich, #T8787) in 1x PBS) for 15min at room temperature, no shaking, then blocking buffer (0.75g Bovine Serum Albumin (Sigma-

Aldrich, #05470) in 25ml 1xPBS) was added and incubated for 1h at room temperature. Blocking buffer was removed and primary antibodies were added in blocking buffer (**Supplementary Table S6**) and incubated overnight at 4°C. Next day primary antibodies were removed and three washes of 5min with IHC Wash Buffer were performed at room temperature. Then, organoids were incubated with secondary antibodies (**Supplementary Table S6**) for 1h at room temperature followed by three washes of 5min with IHC Wash Buffer. Next, Hoechst staining was performed (1:2,000 in 1xPBS) for 5min at room temperature, followed by one wash of 5min with IHC Wash Buffer. Stained organoids were stored at 4°C in IHC Wash Buffer until imaging with inverted microscope (Axio Observer 7, Carl Zeiss Microscopy GmbH) using 350nm and 488nm channels at 10x magnification with identical exposure across all samples.

Neurite outgrowth was quantified using a custom image analysis pipeline implemented in R (version ≥ 4.0) via the DERUNY (Data Engine of Rapid Urban Neural Yields) tool, built with the Shiny and EBImage packages(81). A total of 66 fluorescence images were analyzed (n = 33 per group, WT and MUT), with three images acquired per organoid from 11 organoids in each group. Raw images were loaded and intensity-normalized to the [0, 1] range. For multi-channel images, grayscale conversion was performed using standard luminance- weighted coefficients (R × 0.299, G × 0.587, B × 0.114). No Gaussian pre-smoothing was applied prior to segmentation ($\sigma = 0$).

Binary segmentation of neurite structure was performed using adaptive thresholding (EBImage thresh()), with a sliding window size scaled to image dimensions (bounded between 5 and 21 pixels and set to 1/15 of the shorter image axis) and an adaptive intensity offset of 0.01 (slider value = 1). The resulting binary map was thresholded at its mean value, and connected components were labeled via bwlabel(). Small debris and artefacts were excluded by removing objects below a minimum area threshold of 100 px2, with object areas computed using tabulate() on labeled pixel vectors.

To define the Sholl origin, the soma boundary was manually delineated by clicking a minimum of three points on the binary image overlay. A circle was fit to these points using least-squares algebraic fitting, yielding a center coordinate and soma radius. Concentric Sholl circles were drawn outward from the soma boundary with a start radius padding of 10 pixels and a fixed radial step of 20 pixels (4 µm at 0.2 µm/pixel), up to the maximum radius inscribable within the image frame.

Neurite-circle intersections were counted at each radius using a coverage-aware sampling approach(82). Sampling points were distributed along each circle at an angular density of 0.8 points per pixel of circumference, and pixel intensities at each coordinate were retrieved via bilinear interpolation. Transitions between foreground and background were detected using a dual-threshold hysteresis scheme (hard threshold: 0.6; soft threshold: 0.4), with the total intersection count computed as half the number of detected binary transitions around the full circumference. A fractional coverage metric, f(r), was computed as the proportion of valid (in-frame) sampling points at each radius. The effective arc length at each radius was calculated as $L(r) = f(r) \times 2\pi r \times 0.2$ µm, and normalized intersection density (intersections per µm of arc) was derived by dividing raw intersection counts by L(r). Radii with $L(r) = 0$

were excluded; all remaining radii meeting a minimum coverage threshold of f(r) ≥ 0.05 were retained for analysis and visualization.

Group summary curves were computed per circle ID as the [median or mean] normalized intersection density across all images in each group, with error bars representing ± 1 SEM of per- image values at each circle ID. For visualization, profiles were smoothed using locally weighted regression (LOESS; span = 0.15, weighted by L(r)); this smoothing was applied for display purposes only and was not used in any statistical comparisons. The x-axis was expressed in μm by multiplying circle ID by the radial step size and the spatial calibration (20 px × 0.2 μm/px = 4 μm per circle ID).

Group-level differences in normalized Sholl profiles were assessed using the Mann–Whitney U test (Wilcoxon rank-sum test)(83), applied independently at each circle ID to per-image normalized intersection density values from each group, restricted to rings meeting the minimum coverage threshold (f(r) ≥ 0.05). This rank-based nonparametric test is robust to the outliers and distributional skew common at sparse outer rings and, under similar distribution shapes, tests for differences in group medians.

Neuronal Function and Network Activity

MaxTwo High-Density Microelectrode Array (HD-MEA, Maxwell Biosystems) system was used to record electrophysiological activity of isogenic (WT) and MUT R270X COs at d110 in culture. MaxTwo 6-well electrode plates were prepared according to the manufacturer's protocols. COs were plated on the chips following Brain Organoid Plating protocol (Maxwell Biosystems) with optimizations. Maturation Media was used for preconditioning in the cell culture incubator at 37°C and 5% CO2 for two days. Primary coating was performed with 0.07% PEI (Sigma-Aldrich #P3143) in 1X Borate buffer (Thermo Fisher, #28341) for one hour at 37°C and 5% CO2, followed by three sterile molecular grade water rinses, then all liquid was aspirated, and the electrodes were air-dried completely. Secondary coating was done by adding 500ul of 0.04 mg/mL Laminin (Sigma-Aldrich, #L2020) diluted in Maturation Media to each well/chip, then incubating at 5% CO2 and 37°C overnight. The next day, laminin was removed, and the organoids were plated on the chips (one organoid per chip). Organoids were placed on the chip surface with a P1000 pipette (with previously cut tip) and SUGI absorption spears (AgnThos #18105-01) were used to fully absorb surrounding media. Each organoid was left for three minutes on the chip surface before adding 50μl Maturation Media to encourage organoid's adhesion to the electrodes. Next, the plate was incubated at 37°C and 5% CO2 in the cell culture incubator for two hours before slowly and steady adding an additional 1.2ml of Maturation Media to each well. Media changes were performed three times a week. Recordings of spontaneous electrophysiological activity were performed between days 7 and 21 following organoid plating. MaxLab Live software (MaxWell Biosystems AG, Zurich, Switzerland) was used to perform recordings: electrical activity was measured using the "Activity Scan Assay" with "Full Scan" parameters to record all 26,400 electrodes for 30 s each. A "Network Assay" was then performed to simultaneously measure network activity from 1000 most active electrodes for 300 s. Data for active area, mean firing rate, and mean spike amplitude were exported from the Activity Scan Assay.

Custom code was written to analyze the burst firing metrics using MatLab R2021 and Python. To calculate mean outside burst interspike interval (ISI), the beginning and end timepoints of each burst were determined and a mask was applied to ignore these timeframes. Interspike intervals were then calculated for non-burst-regime timeframes. As a quality control step, chips were excluded from further analysis if the recorded active area was less than 1%, as this level of activity was associated with insufficient network bursting for reliable downstream analysis. This criterion affected only d7 recordings, resulting in WT n = 6 and MUT n = 3 for all d7 electrophysiological metrics; all d14 and d21 recordings met QC thresholds resulting in WT n = 11 and MUT n = 12. WT and MUT groups were compared within each DIV for each electrophysiological metric via one-way ANOVA, and data are presented as mean ± SEM.

AAV packaging and transduction

AAV plasmids carrying either N-terminal dCas9 or C-terminal dCas9-GFP were packaged using AAV-293 cells in AAV-293 media (DMEM (Corning, #10013CV) with 10% Fetal Bovine Serum (Corning, #35-010CV), 1% Penicillin-Streptomycin (Corning, #30-002-CI), 1% L-Glutamine (Corning, #25-005-CI). Cells were transfected with 317.35ug transfer plasmid, 317.35ug AAV2/9 (Addgene #112865), and 634.5ug pAdDeltaF6, in Jetprime buffer with Jetprime transfection reagent. Full media changed was performed 24 hours after transfection and AAV was purified and concentrated following an optimized version of a previously published AAV production protocol(84)(85). Briefly, cells were scraped off and collected in supernatant into 50mL conical tubes, span down at 1500rpm for 5 minutes. The supernatant was collected in new bottles with 25% final concentration of PEG 8000 (Polyethylene glycol) (bioWORLD) and stored at 4°C overnight for AAV precipitation. The cell pellets were resuspended in 4mL of Salt Activated Nuclease (SAN) (4ul/mL, Sigma Aldrich) + SAN digestion buffer (29.22g of NaCl + 4.85g of Tris Base + 2.03g $MgCl2•6H2O$ to a 1L bottle of Molecular Water) and incubated at 37°C for 1 hour then stored at 4°C. The next day, the PEG precipitated solution was centrifuged at 3900rpm for 30 minutes to pellet the AAV, then resuspended with 1mL SAN + SAN digestion buffer and combined with the lysed cell pellets. AAV was then incubated at 37°C for 1 hour and span down at 2000rpm. The supernatant was then used for ultracentrifugation. Previously stored AAV lysate supernatant was added on top of the iodixanol gradient (15%, 25%, 40%, and 60% layer) and ultracentrifuged (Beckman Coulter Optima L-90K Ultracentrifuge) at 69,000rpm, for 1 hour. AAV lysate in the 40% layer was collected. The AAV product was purified and concentrated using Vivaspin 20 (Sartorius) with Ringer's Solution (Thermo Scientific, #AAJ67572AP) according to the manufacturer's instruction and final volume of purified AAV between 0.5-1mL was achieved per construct. AAVs were titrated by qPCR (Takara, #6233). AAVs were then stored in the 4°C for up to 3 months or in the − 80°C for up to a year. AAV9 vectors were produced and purified using iodixanol gradient ultracentrifugation and titrated by qPCR (Takara).

For AAV-GFP transduction: Transduction was performed in COs established from RTT patient-derived NSC lines, both WT and MUT organoid lines at 120 days in culture. Briefly, 5 organoids of similar size (~ 2000µm) were pooled together into a 1.5ml Eppendorf tube and transduced with either $1x10^{11}$ vg, $1x10^{12}$ vg or $1x10^{13}$ vg/tube in 300µl Maturation Media for 6h at 37°C cell incubator in a 10cm dish (with tube's

cap opened inside the dish). Then the total volume in the tube was brought up to 600µl and transduction continued overnight at 37°C cell incubator. Next day, the whole content of the tube (including organoids) was moved to a 6-well Ultra-Low Attachment plate (Corning) in 3ml of Maturation Media per well for the next 24h. After, a whole media change was performed to remove virus from the media, and organoids were cultured for total of 24 days post-transduction with 3 media changes per week. At day 24 post-transduction, gDNA was isolated from single organoids (Zymo Research, #D3025). Quantitative PCR (qPCR) was performed using: 5ng of gDNA per reaction, 5 µM of primers targeting endogenous human GAPDH and transgenic GFP (**Supplementary Table S7**), and SYBR Green Master Mix (Thermo Fisher Scientific, #A46109) were used for quantitative PCR with the StepOne Plus Real-Time PCR system (Thermo Fisher Scientific). qPCR was performed in technical duplicates. Relative expression analysis was calculated as the delta CT between endogenous human GAPDH and transgenic GFP and reported as relative viral genomes (relative vg).

For the immunocytochemistry, COs were processed following previously published protocol for organoid clearance(86) and ICC was performed using 3D Cell Culture Clearing/Staining Kit (CytoVista, #V11325). Imaging was performed using inverted microscope (Axio Observer 7, Carl Zeiss Microscopy GmbH) at 20x magnification, using Z-stack at equal Z-range (76 μm), and 350nm, 488nm, and 647nm channels. Final photos were obtained through Maximum Intensity Projection (MIP) (ZEN 2.5 pro software). All images were acquired and processed using identical settings.

Limitations of the study

While this study provides great insights into modeling Rett syndrome using patient-derived COs, it is important to consider several limitations of this study. First, studied COs are still an *in vitro* model, and only partially recapitulate the *in vivo* brain physiology, lacking aspect of organ-level complexity of the brain including limitation to cortical-like tissue, lack of vascularization, full cellular diversity, and complex circuit formation, which may limit the extent to which observed phenotypes fully recapitulate human neurodevelopment and RTT pathology. Second, although isogenic lines were used to control for genetic background, the study focuses on a single *MECP2* mutation (R270X), and therefore the application of these findings across other RTT variants remains to be established. Third, variability inherent to organoid culture, including batch-to-batch differences and heterogeneity in cellular composition, although shown to be below significance in this study, still may contribute to experimental variability despite efforts to standardize differentiation and maturation protocols. Additionally, although COs were cultured to relatively advanced neuronal maturation stages, prior studies suggest that they primarily model early human brain development (prenatal neocortex). In this context, the phenotypes described here provide insight into neurodevelopmental aspects of MECP2 dysfunction, while their exact relationship to later postnatal stages in RTT patients remains to be further explored in the future. An additional limitation of the electrophysiological analysis is that RSB-like events were identified from representative traces rather than a predefined quantitative burst-classification framework. Therefore, the current data support altered burst organization and increased inter-burst spiking in MUT organoids, but do not yet establish a definitive RSB phenotype. Finally, although this study identifies transcriptional and functional alterations

associated with MECP2 loss, the mechanistic pathways underlying these changes were not fully explored and will require further investigation. Future studies incorporating additional patient iPSC lines, extended maturation, and *in vivo* validation will be important to strengthen this model's capability to recapitulate patient's pathology.

Lead contact

Any request for further information and resources should be directed to and will be fulfilled by the lead contact, Kyle Fink, PhD (kdfink@health.ucdavis.edu).

Materials availability

This study did not generate new unique reagents.

Declarations

Data and code availability

Sequence data generated for this study can be found using the BioProject Accession Number: PRJNA1454517. All scripts used in the RNA-seq analysis can be found here:

https://github.com/vhaghani26/Fink_Klaudia_RNAseq_2026.git

Scripts and instructions on how to download and use DERUNY application for neurite outgrowth quantification can be accessed through GitHub upon publication:

https://github.com/voytsyshynbio/Sholl-Analysis.git

Acknowledgements

We thank Rett Syndrome Research Trust for providing funding for this study. We thank Junjing Jia, PhD at Stem Cell Core Facility at University of California Davis for assistance with culturing and expansion of the iPSCs.

Authors contributions

KMB: Conceptualization; Methodology; Investigation; Formal analysis; Visualization; Data Curation; Writing- original draft; Writing - review and editing. **IYV:** Methodology; Investigation; Software; Formal analysis; Writing - review and editing. **VH:** Formal analysis; Software; Data curation; Visualization; Writing - review and editing. **TF:** Formal analysis; Visualization; Writing - review and editing. **MS:** Methodology; Resources; Writing - review and editing. **CL:** Writing - review and editing. **PB:** Conceptualization; Writing - review and editing. **RBS:** Resources; Writing - review and editing. **JANMH:** Conceptualization; Formal analysis; Writing - review and editing. **KDF:** Conceptualization; Supervision; Project Administration; Funding acquisition; Writing- review and editing.

Declaration of interests

Nothing to Disclose.

Declaration of generative AI and AI-assisted technologies in the writing process

During the preparation of this work, the authors used ChatGPT to improve language clarity and readability. All content was reviewed and edited by the authors, who take full responsibility for the final version.

References

1. Jeffrey L. Neul, Kaufmann WE, Glaze DG, Christodoulou J, Clarke AJ, Bahi-Buisson N, et al. Rett syndrome: Revised diagnostic criteria and nomenclature. Ann Neurol. 2010 Dec;68(6):944–50. doi:10.1002/ana.22124
2. Amir RE, Van Den Veyver IB, Wan M, Tran CQ, Francke U, Zoghbi HY. Rett syndrome is caused by mutations in X-linked MECP2, encoding methyl-CpG-binding protein 2. Nat Genet. 1999 Oct;23(2):185–8. doi:10.1038/13810
3. Lyst MJ, Bird A. Rett syndrome: a complex disorder with simple roots. Nat Rev Genet. 2015 May;16(5):261–75. doi:10.1038/nrg3897
4. Shahbazian MD. Insight into Rett syndrome: MeCP2 levels display tissue- and cell-specific differences and correlate with neuronal maturation. Hum Mol Genet. 2002 Jan 1;11(2):115–24. doi:10.1093/hmg/11.2.115
5. Nan X, Ng HH, Johnson CA, Laherty CD, Turner BM, Eisenman RN, et al. Transcriptional repression by the methyl-CpG-binding protein MeCP2 involves a histone deacetylase complex. Nature. 1998 May;393(6683):386–9. doi:10.1038/30764
6. Guy J, Cheval H, Selfridge J, Bird A. The Role of MeCP2 in the Brain. Annu Rev Cell Dev Biol. 2011 Nov 10;27(1):631–52. doi:10.1146/annurev-cellbio-092910-154121
7. Percy AK, Neul JL, Ananth A, Benke TA, Marsh ED. Symptom Onset in Classic Rett Syndrome: Analysis of Initial Clinical Severity Scale Entries. Ann Child Neurol Soc. 2025 Sep;3(3):152–7. doi:10.1002/cns3.70017
8. Hagberg B, Goutières F, Hanefeld F, Rett A, Wilson J. Rett syndrome: Criteria for inclusion and exclusion. Brain Dev. 1985 Jan;7(3):372–3. doi:10.1016/S0387-7604(85)80048-6
9. Rett A. [On a unusual brain atrophy syndrome in hyperammonemia in childhood]. Wien Med Wochenschr 1946. 1966 Sep 10;116(37):723–6. PubMed PMID: 5300597.
10. Nan X, Campoy FJ, Bird A. MeCP2 Is a Transcriptional Repressor with Abundant Binding Sites in Genomic Chromatin. Cell. 1997 Feb;88(4):471–81. doi:10.1016/S0092-8674(00)81887-5

11. Meehan R, Lewis JD, Bird AP. Characterization of MeCP2, a vertebrate DNA binding protein with affinity for methylated DNA. Nucleic Acids Res. 1992;20(19):5085–92. doi:10.1093/nar/20.19.5085
12. Guy J, Hendrich B, Holmes M, Martin JE, Bird A. A mouse Mecp2-null mutation causes neurological symptoms that mimic Rett syndrome. Nat Genet. 2001 Mar;27(3):322–6. doi:10.1038/85899
13. Chen RZ, Akbarian S, Tudor M, Jaenisch R. Deficiency of methyl-CpG binding protein-2 in CNS neurons results in a Rett-like phenotype in mice. Nat Genet. 2001 Mar;27(3):327–31. doi:10.1038/85906
14. Guy J, Gan J, Selfridge J, Cobb S, Bird A. Reversal of Neurological Defects in a Mouse Model of Rett Syndrome. Science. 2007 Feb 23;315(5815):1143–7. doi:10.1126/science.1138389
15. Mok RSF, Zhang W, Sheikh TI, Pradeepan K, Fernandes IR, DeJong LC, et al. Wide spectrum of neuronal and network phenotypes in human stem cell-derived excitatory neurons with Rett syndrome-associated MECP2 mutations. Transl Psychiatry. 2022 Oct 18;12(1):450. doi:10.1038/s41398-022-02216-1
16. Pradeepan KS, McCready FP, Wei W, Khaki M, Zhang W, Salter MW, et al. Calcium-Dependent Hyperexcitability in Human Stem Cell–Derived Rett Syndrome Neuronal Networks. Biol Psychiatry Glob Open Sci. 2024 Mar;4(2):100290. doi:10.1016/j.bpsgos.2024.100290
17. Marchetto MCN, Carromeu C, Acab A, Yu D, Yeo GW, Mu Y, et al. A Model for Neural Development and Treatment of Rett Syndrome Using Human Induced Pluripotent Stem Cells. Cell. 2010 Nov;143(4):527–39. doi:10.1016/j.cell.2010.10.016
18. Farra N, Zhang WB, Pasceri P, Eubanks JH, Salter MW, Ellis J. Rett syndrome induced pluripotent stem cell-derived neurons reveal novel neurophysiological alterations. Mol Psychiatry. 2012 Dec;17(12):1261–71. doi:10.1038/mp.2011.180
19. Ananiev G, Williams EC, Li H, Chang Q. Isogenic Pairs of Wild Type and Mutant Induced Pluripotent Stem Cell (iPSC) Lines from Rett Syndrome Patients as In Vitro Disease Model. Wutz A, editor. PLoS ONE. 2011 Sep 26;6(9):e25255. doi:10.1371/journal.pone.0025255
20. Yasui DH, Gonzales ML, Aflatooni JO, Crary FK, Hu DJ, Gavino BJ, et al. Mice with an isoform-ablating Mecp2 exon 1 mutation recapitulate the neurologic deficits of Rett syndrome. Hum Mol Genet. 2014 May 1;23(9):2447–58. doi:10.1093/hmg/ddt640
21. Goffin D, Allen M, Zhang L, Amorim M, Wang ITJ, Reyes ARS, et al. Rett syndrome mutation MeCP2 T158A disrupts DNA binding, protein stability and ERP responses. Nat Neurosci. 2012 Feb;15(2):274–83. doi:10.1038/nn.2997
22. Shahbazian MD, Young JI, Yuva-Paylor LA, Spencer CM, Antalffy BA, Noebels JL, et al. Mice with Truncated MeCP2 Recapitulate Many Rett Syndrome Features and Display Hyperacetylation of Histone H3. Neuron. 2002 Jul;35(2):243–54. doi:10.1016/S0896-6273(02)00768-7
23. Sharifi O, Haghani V, Neier KE, Fraga KJ, Korf I, Hakam SM, et al. Sex-specific single cell-level transcriptomic signatures of Rett syndrome disease progression. Commun Biol. 2024 Oct 10;7(1):1292. doi:10.1038/s42003-024-06990-0

24. Kishi N, Macklis JD. MECP2 is progressively expressed in post-migratory neurons and is involved in neuronal maturation rather than cell fate decisions. Mol Cell Neurosci. 2004 Nov;27(3):306–21. doi:10.1016/j.mcn.2004.07.006
25. Belichenko PV, Wright EE, Belichenko NP, Masliah E, Li HH, Mobley WC, et al. Widespread changes in dendritic and axonal morphology in *Mecp2* -mutant mouse models of rett syndrome: Evidence for disruption of neuronal networks. J Comp Neurol. 2009 May 20;514(3):240–58. doi:10.1002/cne.22009
26. Tian A, Muffat J, Li Y. Studying Human Neurodevelopment and Diseases Using 3D Brain Organoids. J Neurosci. 2020 Feb 5;40(6):1186–93. doi:10.1523/JNEUROSCI.0519-19.2019
27. Centeno EGZ, Cimarosti H, Bithell A. 2D versus 3D human induced pluripotent stem cell-derived cultures for neurodegenerative disease modelling. Mol Neurodegener. 2018 Dec;13(1):27. doi:10.1186/s13024-018-0258-4
28. Hodge RD, Bakken TE, Miller JA, Smith KA, Barkan ER, Graybuck LT, et al. Conserved cell types with divergent features in human versus mouse cortex. Nature. 2019 Sep 5;573(7772):61–8. doi:10.1038/s41586-019-1506-7
29. Loomba S, Straehle J, Gangadharan V, Heike N, Khalifa A, Motta A, et al. Connectomic comparison of mouse and human cortex. Science. 2022 Jul 8;377(6602):eabo0924. doi:10.1126/science.abo0924
30. Denayer T, Stöhr T, Roy MV. Animal models in translational medicine: Validation and prediction. Eur J Mol Clin Med. 2014 Aug 27;2(1):5. doi:10.1016/j.nhtm.2014.08.001
31. Granzotto A, Vissel B, Sensi SL. Lost in translation: Inconvenient truths on the utility of mouse models in Alzheimer's disease research. eLife. 2024 Sep 27;13:e90633. doi:10.7554/eLife.90633
32. Lampart FL, Iber D, Doumpas N. Organoids in high-throughput and high-content screenings. Front Chem Eng. 2023 Mar 21;5:1120348. doi:10.3389/fceng.2023.1120348
33. Eiraku M, Watanabe K, Matsuo-Takasaki M, Kawada M, Yonemura S, Matsumura M, et al. Self-Organized Formation of Polarized Cortical Tissues from ESCs and Its Active Manipulation by Extrinsic Signals. Cell Stem Cell. 2008 Nov;3(5):519–32. doi:10.1016/j.stem.2008.09.002
34. Lancaster MA, Knoblich JA. Generation of cerebral organoids from human pluripotent stem cells. Nat Protoc. 2014 Oct;9(10):2329–40. doi:10.1038/nprot.2014.158
35. Quadrato G, Nguyen T, Macosko EZ, Sherwood JL, Min Yang S, Berger DR, et al. Cell diversity and network dynamics in photosensitive human brain organoids. Nature. 2017 May 4;545(7652):48–53. doi:10.1038/nature22047
36. Renner H, Grabos M, Becker KJ, Kagermeier TE, Wu J, Otto M, et al. A fully automated high-throughput workflow for 3D-based chemical screening in human midbrain organoids. eLife. 2020 Nov 3;9:e52904. doi:10.7554/eLife.52904
37. Urrestizala-Arenaza N, Cerchio S, Cavaliere F, Magliaro C. Limitations of human brain organoids to study neurodegenerative diseases: a manual to survive. Front Cell Neurosci. 2024 Jul 9;18:1419526. doi:10.3389/fncel.2024.1419526

38. Gibson JH, Slobedman B, Kn H, Williamson SL, Minchenko D, El-Osta A, et al. Downstream targets of methyl CpG binding protein 2 and their abnormal expression in the frontal cortex of the human Rett syndrome brain. BMC Neurosci. 2010 Dec;11(1):53. doi:10.1186/1471-2202-11-53
39. Kahanovitch U, Cuddapah VA, Pacheco NL, Holt LM, Mulkey DK, Percy AK, et al. MeCP2 Deficiency Leads to Loss of Glial Kir4.1. eneuro. 2018 Jan;5(1):ENEURO.0194-17.2018. doi:10.1523/ENEURO.0194-17.2018
40. Großer E, Hirt U, Janc OA, Menzfeld C, Fischer M, Kempkes B, et al. Oxidative burden and mitochondrial dysfunction in a mouse model of Rett syndrome. Neurobiol Dis. 2012 Oct;48(1):102–14. doi:10.1016/j.nbd.2012.06.007
41. Buchovecky CM, Turley SD, Brown HM, Kyle SM, McDonald JG, Liu B, et al. A suppressor screen in Mecp2 mutant mice implicates cholesterol metabolism in Rett syndrome. Nat Genet. 2013 Sep;45(9):1013–20. doi:10.1038/ng.2714
42. Sadhu C, Lyons C, Oh J, Jagadeeswaran I, Gray SJ, Sinnett SE. The Efficacy of a Human-Ready miniMECP2 Gene Therapy in a Pre-Clinical Model of Rett Syndrome. Genes. 2023 Dec 24;15(1):31. doi:10.3390/genes15010031
43. Ross PD, Gadalla KKE, Thomson SR, Selfridge J, Bahey NG, Benito J, et al. Self-regulating gene therapy ameliorates phenotypes and overcomes gene dosage sensitivity in a mouse model of Rett syndrome. Sci Transl Med. 2025 Apr 2;17(792):eadq3614. doi:10.1126/scitranslmed.adq3614
44. Paşca AM, Sloan SA, Clarke LE, Tian Y, Makinson CD, Huber N, et al. Functional cortical neurons and astrocytes from human pluripotent stem cells in 3D culture. Nat Methods. 2015 Jul;12(7):671–8. doi:10.1038/nmeth.3415
45. Quadrato G, Nguyen T, Macosko EZ, Sherwood JL, Min Yang S, Berger DR, et al. Cell diversity and network dynamics in photosensitive human brain organoids. Nature. 2017 May 4;545(7652):48–53. doi:10.1038/nature22047
46. Ha J, Kang JS, Lee M, Baek A, Kim S, Chung SK, et al. Simplified Brain Organoids for Rapid and Robust Modeling of Brain Disease. Front Cell Dev Biol. 2020 Oct 28;8:594090. doi:10.3389/fcell.2020.594090
47. Gomes AR, Fernandes TG, Vaz SH, Silva TP, Bekman EP, Xapelli S, et al. Modeling Rett Syndrome With Human Patient-Specific Forebrain Organoids. Front Cell Dev Biol. 2020 Dec 10;8:610427. doi:10.3389/fcell.2020.610427
48. Pitcher MR, Herrera JA, Buffington SA, Kochukov MY, Merritt JK, Fisher AR, et al. Rett syndrome like phenotypes in the R255X Mecp2 mutant mouse are rescued by MECP2 transgene. Hum Mol Genet. 2015 May 1;24(9):2662–72. doi:10.1093/hmg/ddv030
49. Yusufzai TM. Functional consequences of Rett syndrome mutations on human MeCP2. Nucleic Acids Res. 2000 Nov 1;28(21):4172–9. doi:10.1093/nar/28.21.4172
50. Guy J, Alexander-Howden B, FitzPatrick L, DeSousa D, Koerner MV, Selfridge J, et al. A mutation-led search for novel functional domains in MeCP2. Hum Mol Genet. 2018 Jul 15;27(14):2531–45. doi:10.1093/hmg/ddy159

51. Gibson JH, Slobedman B, Kn H, Williamson SL, Minchenko D, El-Osta A, et al. Downstream targets of methyl CpG binding protein 2 and their abnormal expression in the frontal cortex of the human Rett syndrome brain. BMC Neurosci. 2010 Dec;11(1):53. doi:10.1186/1471-2202-11-53
52. Huber A, Sarne V, Beribisky AV, Ackerbauer D, Derdak S, Madritsch S, et al. Generation and Characterization of a Human Neuronal In Vitro Model for Rett Syndrome Using a Direct Reprogramming Method. Stem Cells Dev. 2024 Mar;33(5–6):128–42. doi:10.1089/scd.2023.0233
53. Sharifi O, Neier KE, Valenzuela A, Torres CG, Korf I, Lein PJ, et al. Female cortical cellular mosaicism underlies shared MeCP2 and PCB impacted gene pathways [Internet]. Systems Biology; 2025 [cited 2026 May 21]. Available from: http://biorxiv.org/lookup/doi/10.1101/2025.05.28.655836 doi:10.1101/2025.05.28.655836
54. Haghani V, Ali SM, Cannizzaro N, Green R, LaSalle JM, Zarbalis K. Excess prenatal folic acid supplementation alters cortical DNA methylation and gene expression networks. Front Nutr. 2025;12:1699376. doi:10.3389/fnut.2025.1699376
55. Martin M. Cutadapt removes adapter sequences from high-throughput sequencing reads. EMBnet.journal. 2011;17(1):10–2.
56. Dobin A, Davis CA, Schlesinger F, Drenkow J, Zaleski C, Jha S, et al. STAR: ultrafast universal RNA-seq aligner. Bioinformatics. 2013 Jan 1;29(1):15–21. doi:10.1093/bioinformatics/bts635
57. Li H, Handsaker B, Wysoker A, Fennell T, Ruan J, Homer N, et al. The Sequence Alignment/Map format and SAMtools. Bioinformatics. 2009 Aug 15;25(16):2078–9. doi:10.1093/bioinformatics/btp352
58. Ewels P, Magnusson M, Lundin S, Käller M. MultiQC: summarize analysis results for multiple tools and samples in a single report. Bioinformatics. 2016 Oct 1;32(19):3047–8. doi:10.1093/bioinformatics/btw354
59. Chen Y, Lun A, Smyth G. From reads to genes to pathways: differential expression analysis of RNA-Seq experiments using Rsubread and the edgeR quasi-likelihood pipeline [version 2; peer review: 5 approved]. F1000Research. 2016;5(1438). doi:10.12688/f1000research.8987.2
60. Ritchie ME, Phipson B, Wu D, Hu Y, Law CW, Shi W, et al. limma powers differential expression analyses for RNA-sequencing and microarray studies. Nucleic Acids Res. 2015 Apr 20;43(7):e47. doi:10.1093/nar/gkv007
61. Robinson MD, McCarthy DJ, Smyth GK. edgeR: a Bioconductor package for differential expression analysis of digital gene expression data. Bioinformatics. 2010 Jan 1;26(1):139–40. doi:10.1093/bioinformatics/btp616 PubMed PMID: 19910308; PubMed Central PMCID: PMC2796818.
62. Kuleshov MV, Jones MR, Rouillard AD, Fernandez NF, Duan Q, Wang Z, et al. Enrichr: a comprehensive gene set enrichment analysis web server 2016 update. Nucleic Acids Res. 2016 Jul 8;44(W1):W90–7. doi:10.1093/nar/gkw377
63. Kluyver T, Ragan-Kelley B, Pérez F, Granger B, Bussonnier M, Frederic J, et al. Jupyter Notebooks - a publishing format for reproducible computational workflows. In: Loizides F, Scmidt B, editors.

Positioning and Power in Academic Publishing: Players, Agents and Agendas [Internet]. Netherlands: IOS Press; 2016. p. 87–90. Available from: https://eprints.soton.ac.uk/403913/

64. R. Core Team. R: A Language and Environment for Statistical Computing [Internet]. R Foundation for Statistical Computing; 2023. Available from: https://www.R-project.org/
65. Kluyver T, Angerer P, Schulz J, Ram K. IRkernel: Native R Kernel for the “Jupyter Notebook” [Internet]. 2024. Available from: https://github.com/irkernel/irkernel
66. Wickham H. ggplot2: Elegant Graphics for Data Analysis [Internet]. New York, NY: Springer; 2009 [cited 2024 Nov 22]. Available from: https://link.springer.com/10.1007/978-0-387-98141-3 doi:10.1007/978-0-387-98141-3
67. Wickham H, Vaughan D, Girlich M. tidyr: Tidy Messy Data [Internet]. 2026. Available from: https://tidyr.tidyverse.org
68. Wickham H, François R, Henry L, Müller K, Vaughan D. dplyr: A Grammar of Data Manipulation [Internet]. 2023. Available from: https://dplyr.tidyverse.org
69. Polars Development Team. Polars: DataFrames powered by a multithreaded, vectorized query engine [Internet]. 2025. Available from: https://github.com/pola-rs/polars
70. McKinney W. Data Structures for Statistical Computing in Python. In: Walt S van der, Millman J, editors. Proceedings of the 9th Python in Science Conference. 2010. p. 56–61. doi:10.25080/Majora-92bf1922-00a
71. Waskom ML. seaborn: statistical data visualization. J Open Source Softw. 2021;6(60):3021. doi:10.21105/joss.03021
72. Hunter JD. Matplotlib: A 2D Graphics Environment. Comput Sci Eng. 2007 May;9(3):90–5. doi:10.1109/MCSE.2007.55
73. Harris CR, Millman KJ, Walt SJ van der, Gommers R, Virtanen P, Cournapeau D, et al. Array programming with NumPy. Nature. 2020 Sep;585(7825):357–62. doi:10.1038/s41586-020-2649-2
74. Lawrence M, Gentleman R, Carey V. rtracklayer: an R package for interfacing with genome browsers. Bioinformatics. 2009 Jul 15;25(14):1841–2. doi:10.1093/bioinformatics/btp328 PubMed PMID: 19468054; PubMed Central PMCID: PMC2705236.
75. Warnes GR, Bolker B, Bonebakker L, Gentleman R, Huber W, Liaw A, et al. gplots: Various R Programming Tools for Plotting Data [Internet]. 2025. Available from: https://github.com/talgalili/gplots
76. Neuwirth E. RColorBrewer: ColorBrewer Palettes [Internet]. 2022. Available from: https://CRAN.R-project.org/package=RColorBrewer
77. Schauberger P, Walker A. openxlsx: Read, Write and Edit xlsx Files [Internet]. 2025. Available from: https://ycphs.github.io/openxlsx/index.html
78. Wickham H, Bryan J. readxl: Read Excel Files [Internet]. 2025. Available from: https://readxl.tidyverse.org

79. Hester J, Bryan J. glue: Interpreted String Literals [Internet]. 2024. Available from: https://glue.tidyverse.org/
80. Slowikowski K. ggrepel: Automatically Position Non-Overlapping Text Labels with “ggplot2” [Internet]. 2026. Available from: https://ggrepel.slowkow.com/
81. Pau G, Fuchs F, Sklyar O, Boutros M, Huber W. EBImage—an R package for image processing with applications to cellular phenotypes. Bioinformatics. 2010 Apr 1;26(7):979–81. doi:10.1093/bioinformatics/btq046
82. Langhammer CG, Previtera ML, Sweet ES, Sran SS, Chen M, Firestein BL. Automated Sholl analysis of digitized neuronal morphology at multiple scales: Whole cell Sholl analysis versus Sholl analysis of arbor subregions. Cytometry A. 2010 Dec;77A(12):1160–8. doi:10.1002/cyto.a.20954
83. Chicco D, Sichenze A, Jurman G. A simple guide to the use of Student’s t-test, Mann-Whitney U test, Chi-squared test, and Kruskal-Wallis test in biostatistics. BioData Min. 2025 Aug 20;18(1):56. doi:10.1186/s13040-025-00465-6
84. Challis RC, Ravindra Kumar S, Chan KY, Challis C, Beadle K, Jang MJ, et al. Systemic AAV vectors for widespread and targeted gene delivery in rodents. Nat Protoc. 2019 Feb;14(2):379–414. doi:10.1038/s41596-018-0097-3
85. Crosson SM, Dib P, Smith JK, Zolotukhin S. Helper-free Production of Laboratory Grade AAV and Purification by Iodixanol Density Gradient Centrifugation. Mol Ther - Methods Clin Dev. 2018 Sep;10:1–7. doi:10.1016/j.omtm.2018.05.001
86. Dekkers JF, Alieva M, Wellens LM, Ariese HCR, Jamieson PR, Vonk AM, et al. High-resolution 3D imaging of fixed and cleared organoids. Nat Protoc. 2019 Jun;14(6):1756–71. doi:10.1038/s41596-019-0160-8

Figures

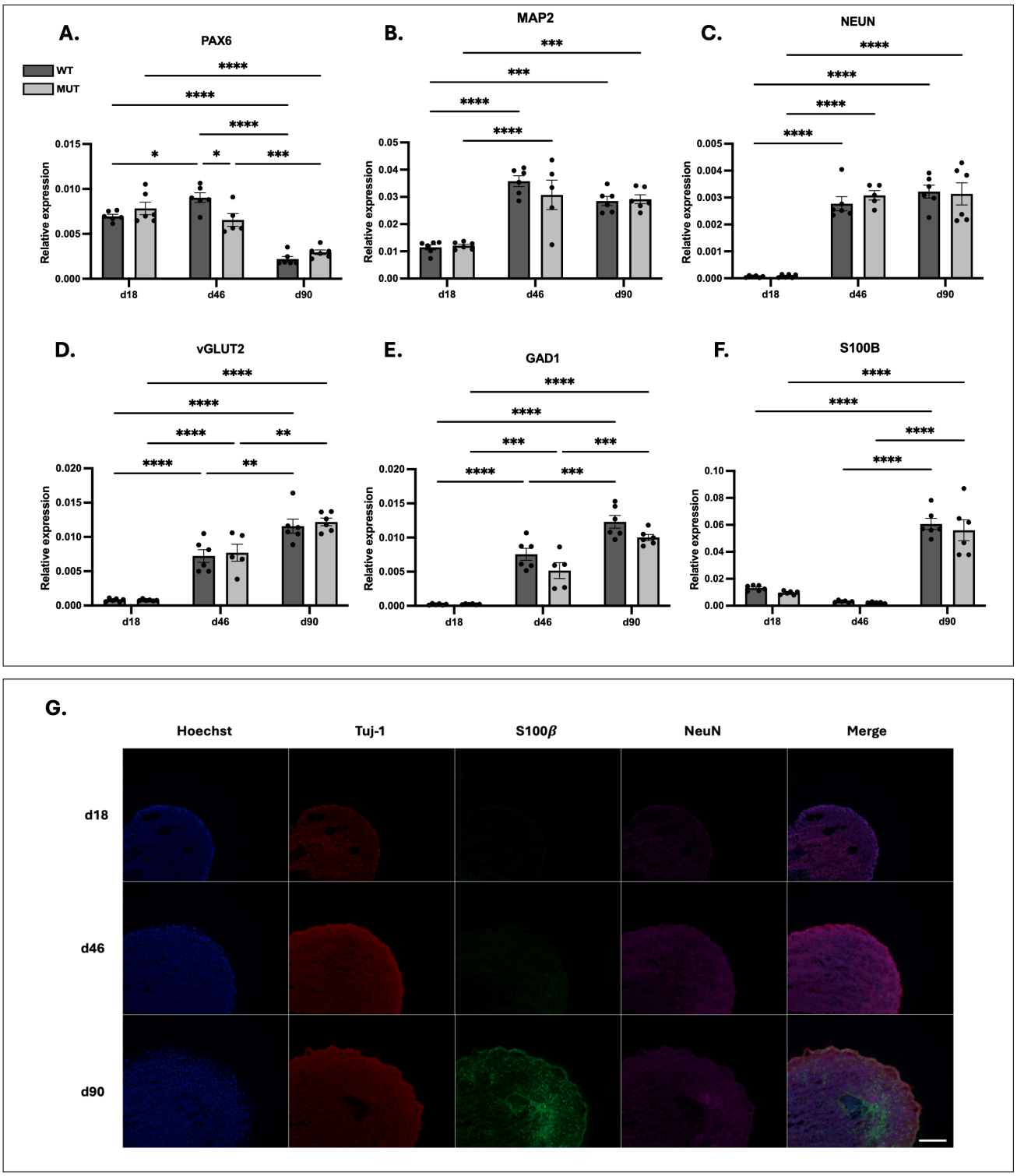


Figure 1

Presence of various neuronal markers in newly established (d18), early maturating (d46) and mature (d90) cerebral organoids. RNA was isolated from WT and MUT organoids and RT-qPCR was performed reveling expression of markers for diverse population of neuronal cells and continued expression of these markers throughout the maturation process confirming the cerebral character of established organoids with PAX6 (A), MAP2 (B), NeuN (C), vGlut2 (D), GAD1 (E), S100β (F). Performed across two

independent batches of COs at d18: NWT=6, NMUT=6; d46: NWT=6, NMUT=5; d90: NWT=6, NMUT=6. Statistical significance assessed using two-way ANOVA, followed by the Šidák's multiple comparisons test, *p < 0.05, **p < 0.01, ***p < 0.001. F. Immunocytochemistry of developing organoids and expression of neuronal markers in newly established (d18), early maturating (d46) and mature (d90) COs. Throughout development and maturation of the isogenic organoids derived from the XaMECP2 WT NSC line, qualitative increase in glia cells (S100β) and mature neurons (NeuN) was observed suggesting increasing cell diversity and gain of mature, post-mitotic neurons with time in the established organoid culture (Zeiss, 10x; scale bar indicates 100µm).

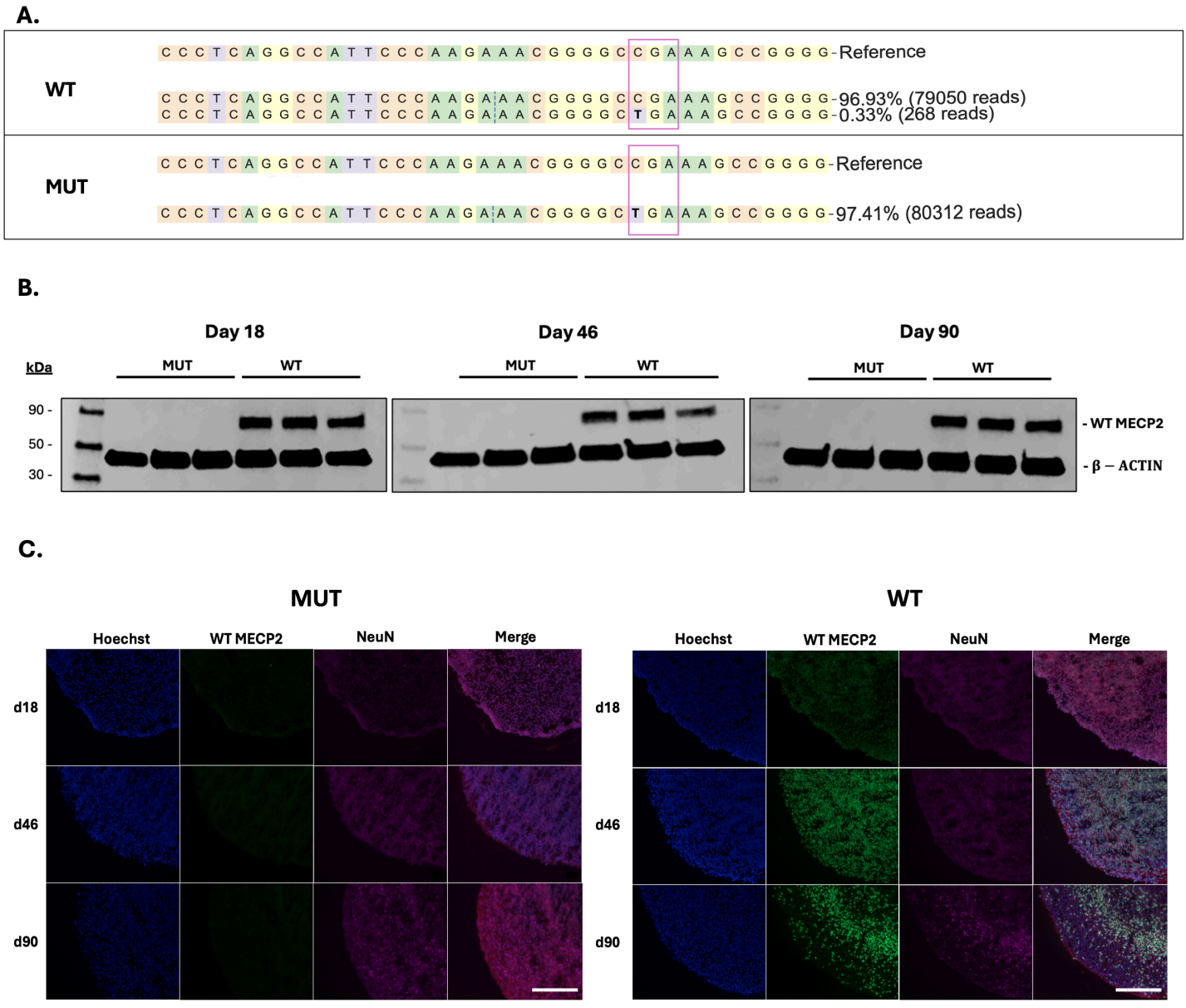


Figure 2

MECP2 expression patterns in clonal cerebral organoids. A. An amplicon Next-Generation Sequencing (NGS) analysis of RTT patient NSCs showing clonal mRNA expression of either WT *MECP2* ($Xa^{MECP2\ WT}$)

or MUT *MECP2* ($Xa^{MECP2\ R270X}$) allele with 2.74% (WT sample) and 2.59% (MUT sample) reads unmapped to either WT or MUT sequences. Data analysis and visualization performed using CRISPResso2.com. **B.** Full length MECP2 protein expression profiles in Western Blot. Consistent presence (in WT COs) and absence (in MUT COs) of full-length MECP2 protein was observed through development in derived COs (using antibody targeting full-length-MECP2). **C.** ICC targeting MECP2 expression in COs. Full-length MECP2 is consistently absent in MUT and present in WT (isogenic) COs through development. In mature WT CO line, MECP2 strongly colocalizes with the mature neuronal marker (NeuN) suggesting MECP2 enrichment in mature neurons within the organoids (10x, Zeiss; scale bars indicate 200μm).

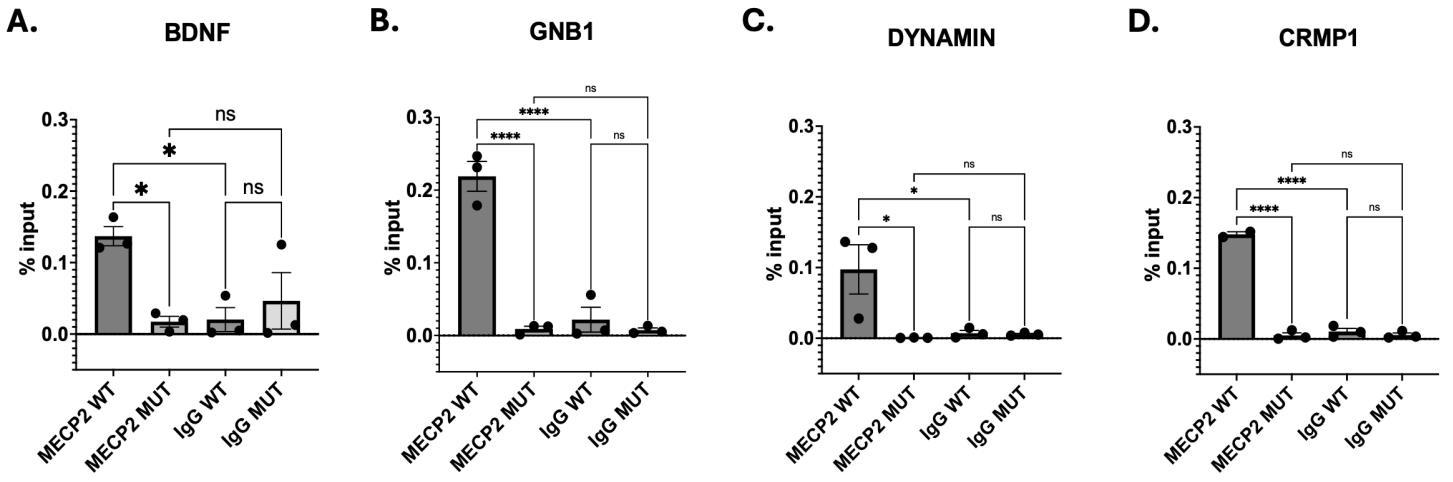


Figure 3

Full-length MECP2 binds known target gene regions in isogenic organoids. ChIP-qPCR was performed using an anti-MECP2 or IgG control antibodies in WT and MUT COs. Enrichment was quantified for four known, and previously identified MECP2-binding loci including *BDNF* (**A**), *GNB1* (**B**), *DYNAMIN*(**C**), and *CRMP1* (**D**) and expressed as percent of input. We observe MECP2 occupancy at all four loci compared to IgG controls in WT COs. No significant enrichment was observed in MUT COs, consistent with loss of C-terminus fragment of MECP2 protein in R270X mutant line. Statistical significance was determined using one-way ANOVA followed by Tukey's multiple comparisons test (*p < 0.05, **p < 0.01, ***p < 0.001, ****p < 0.0001, ns = not significant).

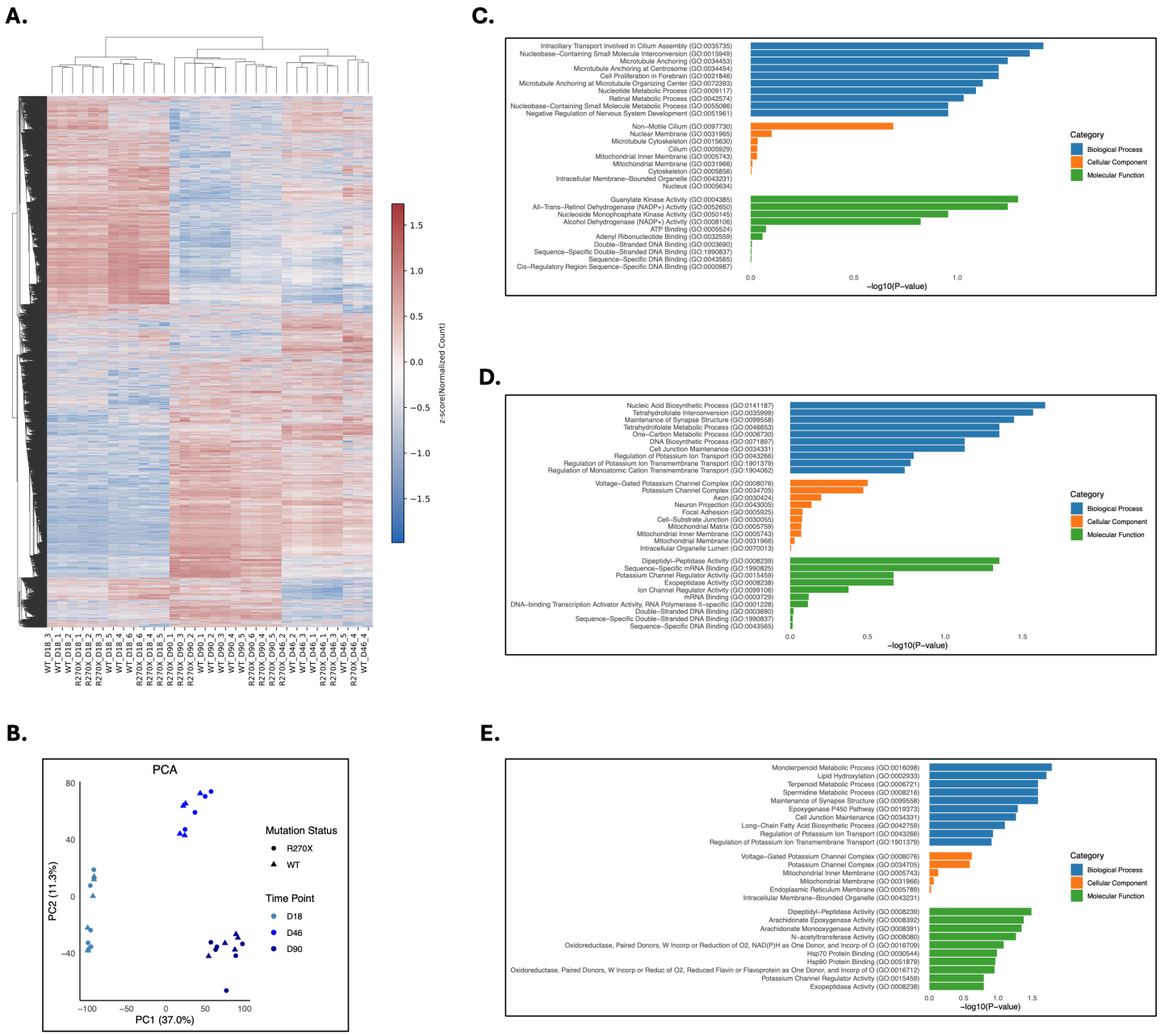


Figure 4

Bulk RNA sequencing of WT and MUT COs at day 18, 46 and 90 in development. Comparison between WT and MUT CO samples show progressive, mutation-driven transcriptomic dysregulations through development. **A.** Heatmap representing DEGs showing clustering of WT and MUT samples according to respective timepoints in development with most distinct transcriptional changes between d18 and d90 samples. **B.** PCA analysis showing visible clustering of the samples at the same timepoints in development across multiple batches of WT and MUT COs, with three distinct clusters for each sampling timepoint. GO enrichment analysis showing enrichment in DEGs associated with dysregulated pathways at day 18 (**C**), day 46 (**D**) and day 90 (**E**) in COs development between WT and MUT COs. Performed across two independent batches of COs at MUT d18 (n = 6), MUT d46 (n = 4), MUT d90 (n = 6), WT d18 (n = 6), WT d46 (n= 5), and WT d90 (n = 5), each N represents a sample pooled form 3-6 COs.

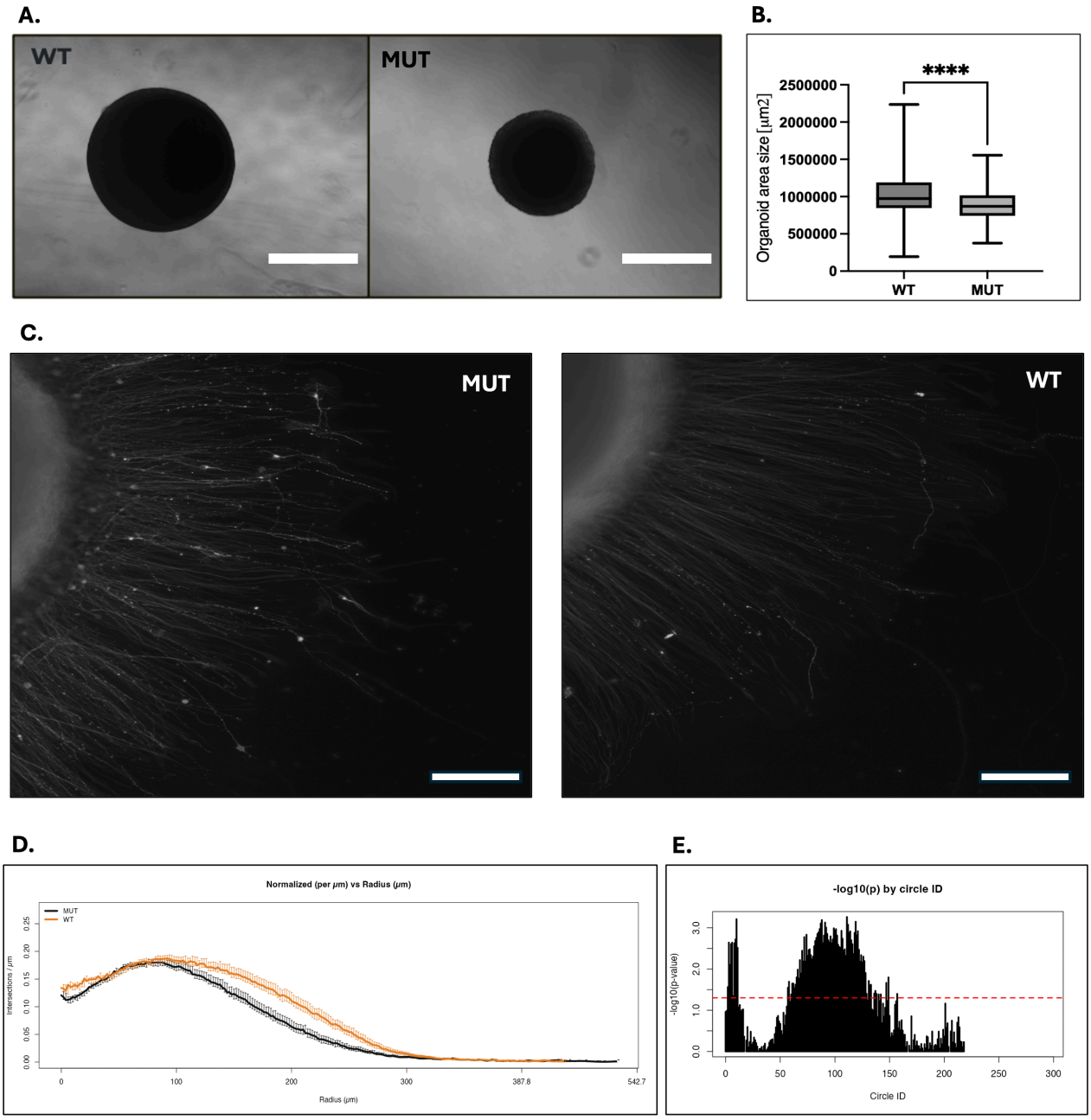


Figure 5

Morphological differences between WT and MUT COs. A. A comparison between WT and MUT CO areas (4x, Evos, Brightfield; Scale bars indicate 750µm). B. Significant difference in organoid area was observed between WT and MUT COs at day 129 in culture. NWT=120 and NMUT=121 COs, across one independent CO aggregation. Data presented as mean ± min–max. Statistical significance was determined using Welch's two-tailed t-test, ****p <0.0001. C. Neurite outgrowth assay. WT and MUT COs were plated separately on PLO-LAM coated culture plates, neurite outgrowth was observed, and ICC was performed using anti-Tuj-1 primary antibody (10x, Zeiss, Scale bars indicate 200µm). D. Neurite outgrowth data was quantified and processed using newly developed DERUNY tool, and structural changes in neuronal outgrowth in MUT vs. WT COs were revealed, suggesting impaired neurite structure in MUT COs. E. Neurite branching differences were assessed with the Mann–Whitney U test. The red line

marks the significance threshold (p = 0.005). A total of 66 fluorescence images were analyzed (n= 33 per group, WT and MUT), with three images acquired per organoid from 11 organoids in each group, across one independent aggregation.

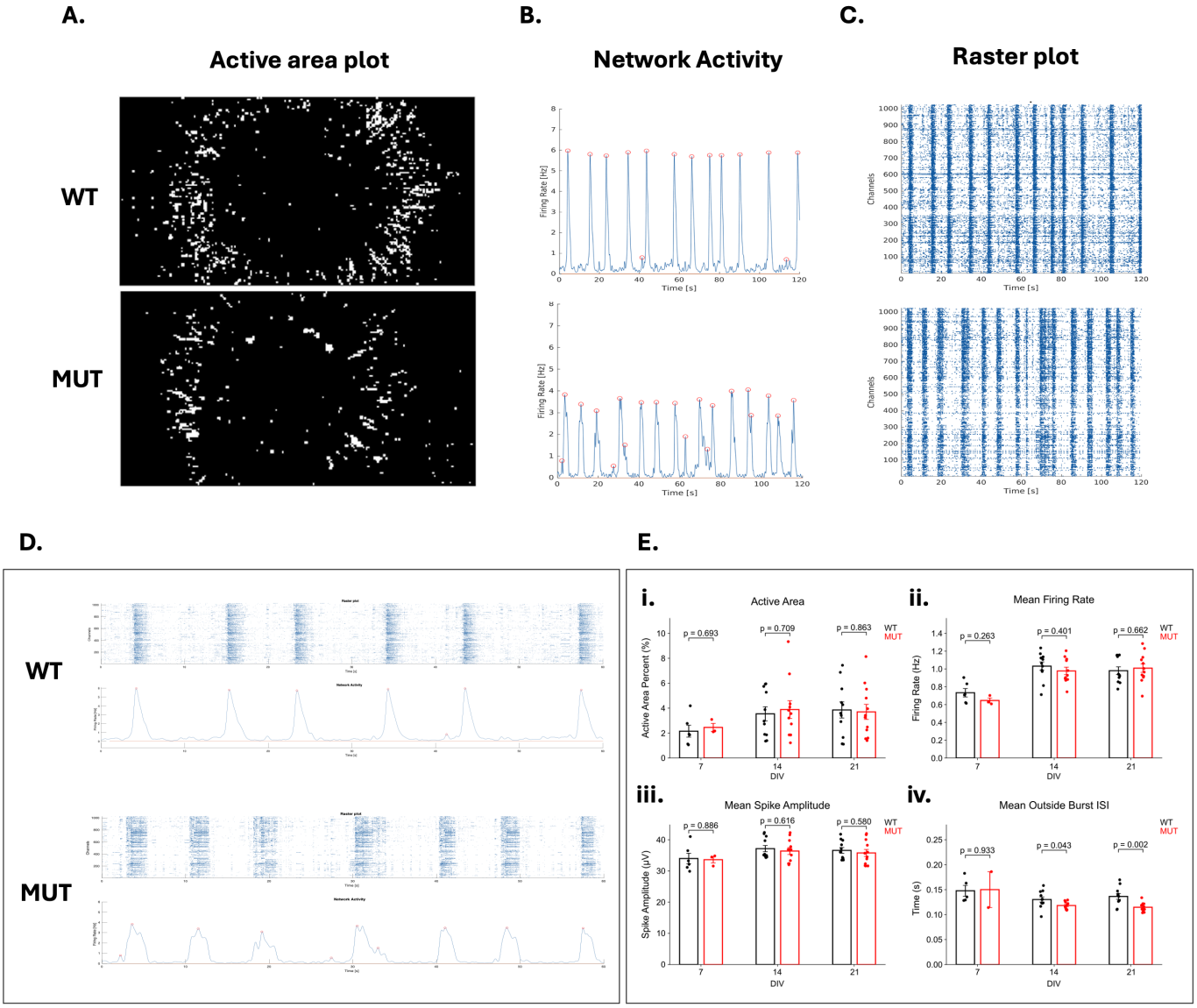


Figure 6

HD-MEA reveals altered burst organization and reduced outside-burst inter-spike interval in MUT COs. Neuronal firing activity of the WT and MUT mature COs (d110 in culture) at DIV7, DIV14 and DIV21 on the chip. Both WT and MUT COs exhibit develop neurite outgrowth (**A**), exhibit spontaneous firing and development of neuronal networks (**B, C**). **D.** Comparison of burst peak shape between WT and MUT COs with visibly impaired, wider bursting pattern in MUT showing altered, RSB-like burst organization. **E.** No difference in active area (DIV7 p=0.693; DIV 14 p=0.709; DIV 21 p=0.863), mean firing rate (DIV 7

p=0.263; DIV 14 p=0.401; DIV21 p=0.662), or mean spike amplitude (DIV7 p=0.886; DIV14 p=0.616; DIV21 p=0.580) is observed over time between WT and MUT COs (**Fig. 6E.i-iii**). Significantly decreased mean outside burst inter-spike-interval in MUT COs at DIV14 (p=0.043) and DIV21 (p=0.002) but not at DIV7 (p=0.933) was observed, consistent with increased spiking outside of burst events as networks matured (**Fig.6E.iv**). Performed across two independent batches of COs at DIV7: N_{WT}= 6 and N_{MUT}= 3, DIV14: N_{WT}= 11 and N_{MUT} =12, DIV21: N_{WT}= 11 and N_{MUT} =12. WT and MUT groups were compared within each DIV for each electrophysiological metric via one-way ANOVA, data presented as mean ± SEM.

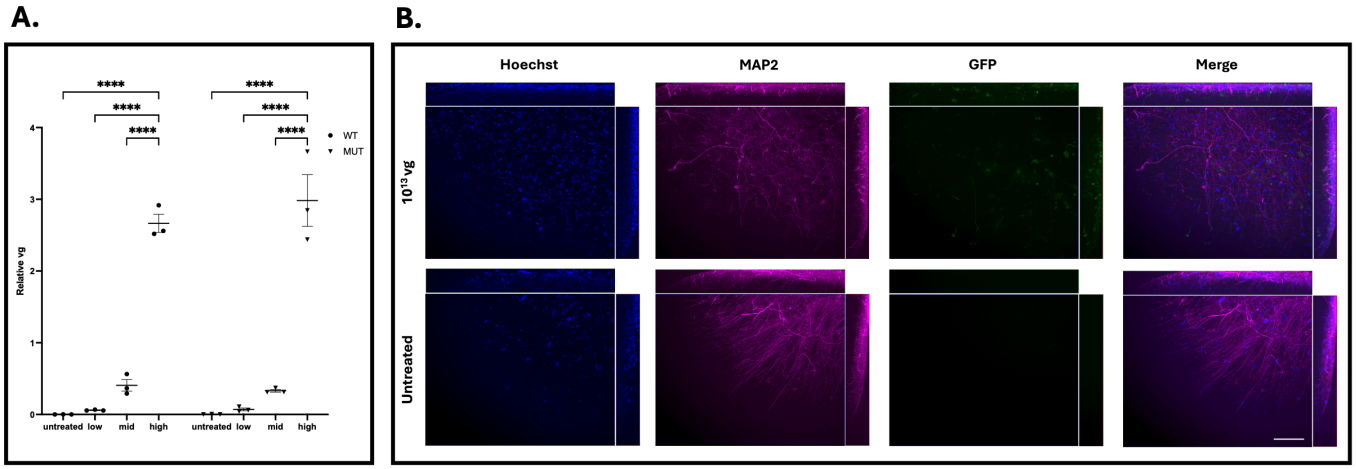


Figure 7

NSC-derived COs transduce with AAV9 in dose-dependent manner. Mature RTT patient-derived WT and MUT COs were transduced for 24 days using three doses, low (1 x 10^{11} vg), mid (1 x 10^{12} vg), or high (1 x 10^{13} vg), of in-house-made and purified AAV9 virus carrying GFP reporter. **A.** Relative GFP signal (relative vg, normalized to GAPDH) was measured in WT and MUT COs across increasing AAV9 doses, revealing significant effect of dose but no effect of genotype (data represented as mean ± SEM, n = 3 per dose. Two-way ANOVA with Šídák's multiple comparisons test).

B. Whole organoid ICC of WT CO high dose-treated (z-stack images, ortholog view) showing distribution of the transgenic GFP protein across organoid structure and colocalization with mature neuronal marker (MAP2), compared to lack of GFP signal in WT CO untreated, supports transduction of neurons in the organoids (10x, Zeiss, Z-stack projection, 76μm slice, scale bar indicates 100μm).

Supplementary Files

This is a list of supplementary files associated with this preprint. Click to download.

- SupplementaltablesSCR.docx
- Graphicalabst.png